A depositional model for hydromagnesite–magnesite playas near Atlin, British Columbia, Canada

IAN M. POWER*, SIOBHAN A. WILSON†, ANNA L. HARRISON*, GREGORY M. DIPPLE*, JENINE MCCUTCHEON‡, GORDON SOUTHAM¶ and PAUL A. KENWARD*
*Department of Earth, Ocean and Atmospheric Sciences, The University of British Columbia, Vancouver, BC V6T 1Z4, Canada (E-mail: ipower@eos.ubc.ca)
†School of Geosciences, Monash University, Clayton, Vic. 3800, Australia
‡Department of Earth Sciences, The University of Western Ontario, London, ON N6A 5B7, Canada
¶School of Earth Sciences, The University of Queensland, Brisbane, St Lucia, Qld 4072, Australia

Associate Editor – Daniel Ariztegui

ABSTRACT

This study formulates a comprehensive depositional model for hydromagnesite–magnesite playas. Mineralogical, isotopic and hydrogeochemical data are coupled with electron microscopy and field observations of the hydromagnesite–magnesite playas near Atlin, British Columbia, Canada. Four surface environments are recognized: wetlands, grasslands, localized mounds (metre-scale) and amalgamated mounds composed primarily of hydromagnesite $[Mg_5(CO_3)_4(OH)_2 \cdot 4H_2O]$, which are interpreted to represent stages in playa genesis. Water chemistry, precipitation kinetics and depositional environment are primary controls on sediment mineralogy. At depth (average ≈ 2 m), Ca–Mg-carbonate sediments overlay early Holocene glaciolacustrine sediments indicating deposition within a lake post-deglaciation. This mineralogical change corresponds to a shift from siliciclastic to chemical carbonate deposition as the supply of fresh surface water (for example, glacier meltwater) ceased and was replaced by alkaline groundwater. Weathering of ultramafic bedrock in the region produces Mg–HCO$_3$ groundwater that concentrates by evaporation upon discharging into closed basins, occupied by the playas. An uppermost unit of Mg-carbonate sediments (hydromagnesite mounds) overlies the Ca–Mg-carbonate sediments. This second mineralogical shift corresponds to a change in the depositional environment from subaqueous to subaerial, occurring once sediments 'emerged' from the water surface. Capillary action and evaporation draw Mg–HCO$_3$ water up towards the ground surface, precipitating Mg-carbonate minerals. Evaporation at the water table causes precipitation of lansfordite $[MgCO_3 \cdot 5H_2O]$ which partially cements pre-existing sediments forming a hardpan. As carbonate deposition continues, the weight of the overlying sediments causes compaction and minor lateral movement of the mounds leading to amalgamation of localized mounds. Radiocarbon dating of buried vegetation at the Ca–Mg-carbonate boundary indicates that there has been *ca* 8000 years of continuous Mg-carbonate deposition at a rate of 0·4 mm yr^{-1}. The depositional model accounts for the many sedimentological, mineralogical and geochemical processes that occur in the four surface environments; elucidating past and present carbonate deposition.

Keywords Carbon storage, depositional model, hydromagnesite, lansfordite, magnesite, playa, Rietveld method, stable isotopes.

INTRODUCTION

Carbonate mineralogy of modern and ancient playas is variable and complex, consequently there remain uncertainties regarding playa genesis. The hydromagnesite–magnesite playas near Atlin, British Columbia, Canada, provide insights into the geochemical conditions that drive Mg-carbonate deposition near the Earth's surface. Carbonate sediments in freshwater systems are of renewed interest because of their relevance to mitigating greenhouse gas emissions. There has been extensive investigation of industrial processes for storing carbon dioxide (CO_2) in Mg-carbonate minerals (e.g. Lackner *et al.*, 1995; Sipilä *et al.*, 2008; Power *et al.*, 2013c) and of processes that produce these minerals under low-temperature and low-pressure conditions similar to those at the Earth's surface (Schuiling & Krijgsman, 2006; Wilson *et al.*, 2006, 2009a; Köhler *et al.*, 2010; Power *et al.*, 2010, 2011, 2013a,b; Renforth & Manning, 2011; Bea *et al.*, 2012; Renforth, 2012; Washbourne *et al.*, 2012; Harrison *et al.*, 2013). The Atlin playas are ideal environments for studying the Mg-carbonate mineral system at Earth's surface conditions, with implications for the long-term stability of sequestered CO_2.

The formation of magnesite at low temperatures is kinetically inhibited and, therefore, numerous metastable hydrated phases are formed (Königsberger *et al.*, 1999; Hänchen *et al.*, 2008). The complexity of the Mg-carbonate system has led to an incomplete understanding of the precipitation of these minerals in natural and industrial systems (Hänchen *et al.*, 2008). Magnesium-carbonate mineral precipitation and phase transformations may depend on temperature, partial pressure of CO_2, Mg concentration and probably other factors (Königsberger *et al.*, 1999; Hänchen *et al.*, 2008; Hopkinson *et al.*, 2012). Hence, numerous environmental conditions must be considered when interpreting sedimentary sequences that are dominated by Mg-carbonate minerals. The knowledge acquired from the present study provides a better understanding of carbonate formation in modern and ancient playas (Cummings, 1940; Grant, 1987; Renaut & Long, 1989; Renaut, 1990, 1993; Spotl & Burns, 1994; Peng *et al.*, 1998; Valero-Garcés *et al.*, 2000; Zedef *et al.*, 2000; Melezhik *et al.*, 2001; Pakzad & Kulke, 2007; Stamatakis *et al.*, 2007; Liutkus & Wright, 2008; Lopez *et al.*, 2008; Alcicek, 2009; Mees *et al.*, 2011; Meister *et al.*, 2011; Last & Last, 2012; McGlue *et al.*, 2012). The depositional model presented in this study may also lend itself to improved interpretation of the environmental requirements for Mg-carbonate deposition in similar environments such as lakes (Braithwaite & Zedef, 1994, 1996; Coshell *et al.*, 1998; Russell *et al.*, 1999; Kaźmierczak *et al.*, 2011).

The objectives of this study were to: (i) quantitatively determine the mineralogical composition of the Atlin playas; (ii) assess mineralogical, hydrogeochemical and isotopic data, with electron microscopy and field observations as they relate to playa genesis; (iii) formulate a depositional model that describes playa genesis; and (iv) estimate the carbonate accumulation rate of Mg-carbonate sediments in the playa.

SITE DESCRIPTION

Hydromagnesite–magnesite playas are found near the town of Atlin in north-western British Columbia (59°34′00″N, 133°42′00″W, elevation = 673·6 m; Fig. 1A). Atlin has a subarctic climate with long winters and mild summers. The average yearly temperature is 0·5°C with January (average temperature = −15·4°C) and July (average temperature = 13·1°C) being the coldest and warmest months of the year, respectively. Atlin receives an average of 193 mm of rainfall and 155 cm of snowfall for a total of 347 mm of liquid precipitation (Environment Canada, n.d.).

In the Atlin region, the geology is primarily ultramafic, consisting of a tectonically emplaced upper mantle section of oceanic lithosphere. The upper mantle section is composed mostly of serpentinite with listwanite (magnesite + quartz) transformed from predominantly harzburgite and minor dunite (Ash & Arksey, 1990; Hansen *et al.*, 2005). Two groups of playas exist immediately east of Atlin. The first of these is referred to in this study as the northern playa, which has nearby small satellite playas (Fig. 1B). The second group, to the south, consists of two playas separated by a ridge, referred to as the south-western playa and south-eastern playa (Fig. 1B). Interest in the playas dates to 1904 when *ca* 200 tons of material, assumed to be hydromagnesite, was shipped to San Francisco in order to assess the merit of pursuing commercial development of the deposit. Formulae of relevant carbonate minerals found in the playas are listed in Table 1. It is also thought that some material was sent to England. An estimated 500 tons of sediment from the northern playa were shipped to Vancouver, British Columbia in 1915 (Young, 1916).
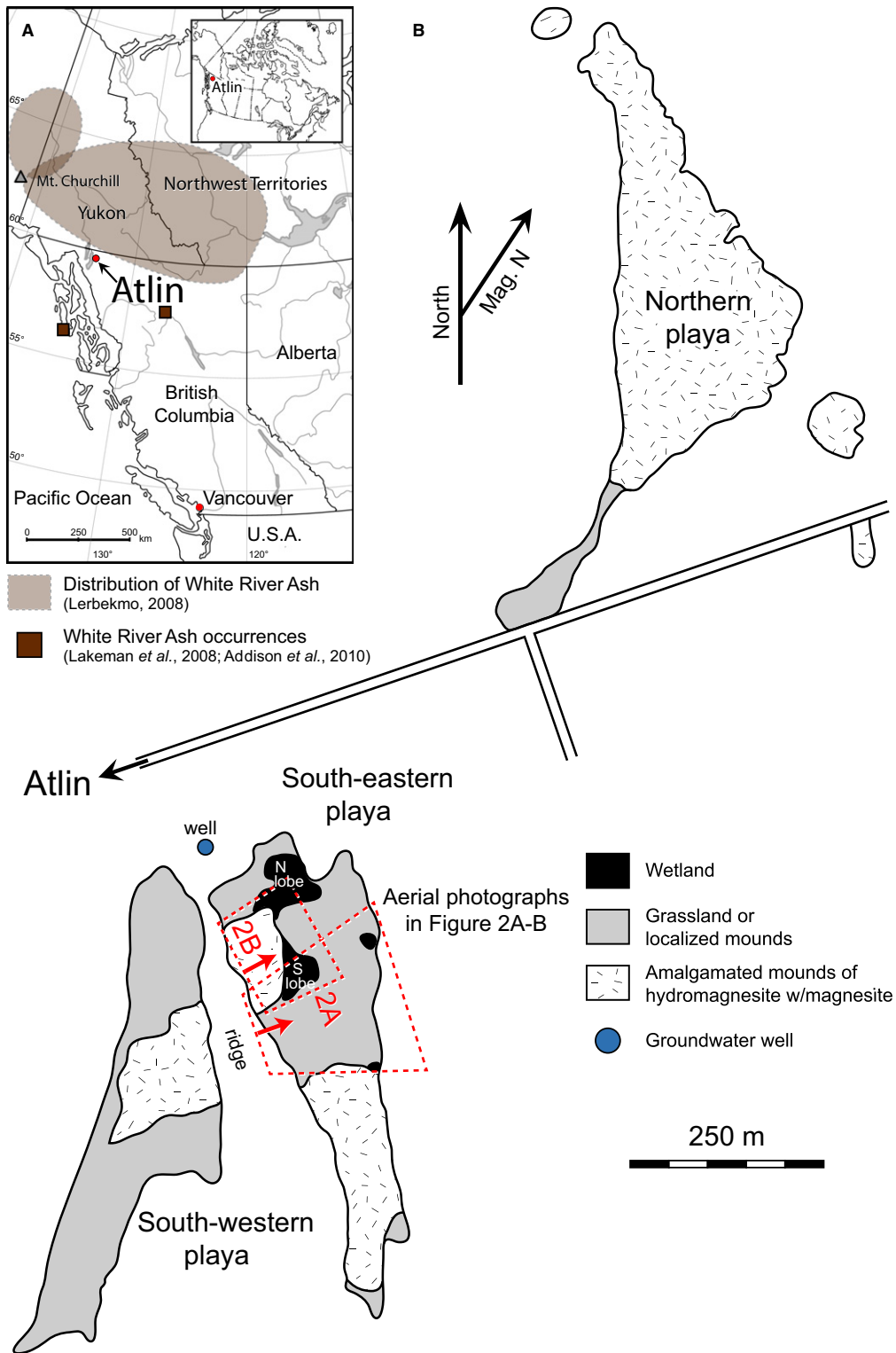
Fig. 1. (A) A map showing the location of Atlin, British Columbia, Canada. The extent of the White River Ash (after Lerbekmo, 2008) is indicated by the shaded area, as well as documented occurrences in the Alaskan pan-handle (Addison *et al.*, 2010) and north-central British Columbia (Lakeman *et al.*, 2008). (B) A map illustrating the northern, south-western and south-eastern playas near Atlin. The approximate positions of the aerial photographs in Fig. 2 are outlined on the map, as well as the location of the groundwater well.

Table 1. Formulae for relevant carbonate minerals in playas.

Mineral name	Formula
Lansfordite	$MgCO_3 \cdot 5H_2O$
Nesquehonite	$MgCO_3 \cdot 3H_2O$
Dypingite	$Mg_5(CO_3)_4(OH)_2 \cdot 5H_2O$
Hydromagnesite	$Mg_5(CO_3)_4(OH)_2 \cdot 4H_2O$
Magnesite	$MgCO_3$
Dolomite	$CaMg(CO_3)_2$
Huntite	$CaMg_3(CO_3)_4$
Ankerite	$Ca(Fe^{2+},Mg,Mn)(CO_3)_2$
Aragonite	$CaCO_3$

The playas were first described and mapped by Young (1916) who also sampled sediments for chemical analysis. Estimates of the size of the deposits were performed by Grant (1987) and their industrial use as fire retardants was assessed by Stamatakis *et al.* (2007). Most recently, the playas have been characterized in the context of a biogeochemical model for CO_2 sequestration focusing on biological pathways for Mg-carbonate precipitation (Power *et al.*, 2007, 2009). The present study focuses on the south-eastern playa, which has four surface environments: wetlands, grasslands, localized mounds and amalgamated mounds (see aerial photograph in Fig. 2A). The majority of sediment sampling was performed in the amalgamated mound, which is adjacent to the main wetland (Fig. 2B). The main wetland has a north and south lobe that may be connected when water levels are high. The south lobe is considerably more shallow (<1 m average depth) than the north lobe (>1 m average depth). The main wetland has a total area of *ca* 0·5 ha and has no natural channelled inflows or outflows; however, a drainage channel was once excavated to lower water levels to prevent flooding of adjacent private property. A few smaller water bodies are also present in the south-eastern playa. Dispersed over some areas of the playas are areas vegetated by grasses, referred to as grasslands. Localized (metre-scale) and amalgamated mounds occupy the majority of the playas. All field work and sampling was conducted during summer months.

METHODS

Field methods

Water sampling
Water samples included spring water from the base of Monarch Mountain that is *ca* 3·5 km to the south-east of the playas, groundwaters from a well and water from the water table during sediment sampling. The well (*ca* 35 m deep and 15·2 cm wide) was located *ca* 50 m from the south-eastern playa (Fig. 1) and was flushed with a minimum of three volumes to obtain representative groundwater. A 50 ml syringe and tygon tubing were used to collect samples from the water table during sediment sampling. Surface water sampling in the south-eastern playa included samples from small ponds and the north and south lobes of the main wetland. A Thermo Scientific® Orion 4-Star portable pH/ISE meter (Thermo Scientific, Waltham, MA, USA) was used to measure pH, and alkalinity was determined by titration with 0·1 N HCl (Lahav *et al.*, 2001). For cation analyses, water samples were filtered into 2 ml borosilicate glass vials using 0·22 μm Millipore Millex® GP sterile syringe filters (Millipore, Billerica, MA, USA) and were acidified to 2% v/v ultrapure nitric acid in the field. For anion and stable isotope analyses ($\delta^{13}C_{DIC}$, δ^2H and $\delta^{18}O$), samples were filtered into 15 ml BD Falcon tubes and TraceClean™ (VWR, Radnor, PA, USA) 40 ml amber borosilicate vials with a septum liner, respectively. All samples were stored at 4°C prior to processing.

Sediment sampling
The majority of sediment sampling was conducted on the amalgamated mound shown in Fig. 2B. A sampling grid was marked using north–south and west–east trending transects and samples were collected every 10 m. Samples (66 in total) were collected from *ca* 5 to 10 cm below the surface to minimize the effect of surface disturbance. The magnesite abundances determined for these near-surface samples were contoured with Golden Software Surfer 8 using the radial basis function for interpolation.

Collection of sediments with depth was performed along a north-trending transect (75 m) at 10 to 25 m intervals, beginning at the outer edge of the playa and extending to near the wetland (Fig. 2B). Samples (116 in total) were collected at various depths (up to 4 m) using an auger at seven locations along this transect that are henceforth referred to as 'sediment profiles 1 to 7' (see Table S1 in the supplementary material). A thermometer was used to measure the temperature of sediments immediately following sampling. Metre sticks and a laser level were used to determine the relative elevations of the sediment profiles.
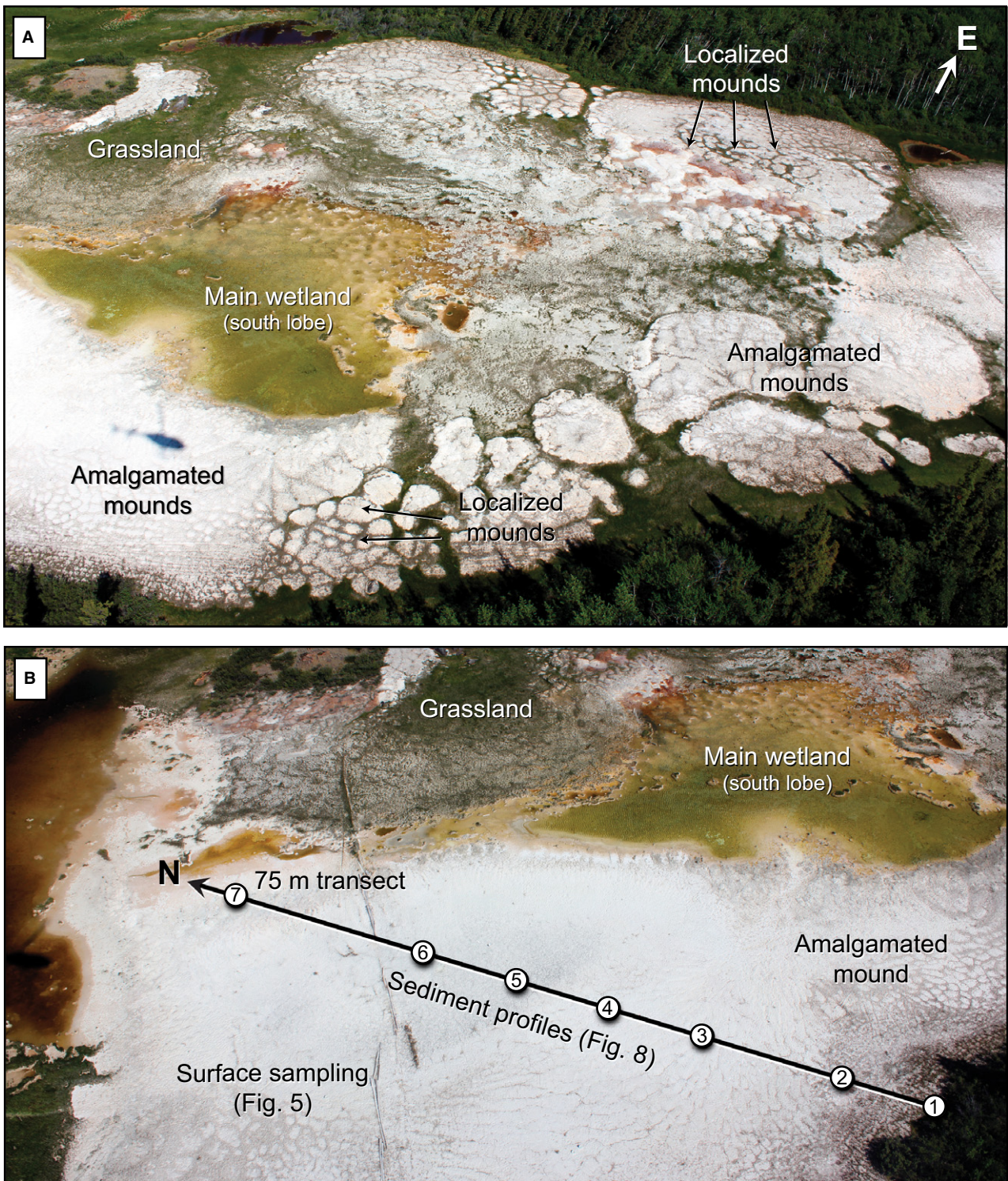
Fig. 2. Aerial photographs of the south-eastern playa; locations are outlined on Fig. 1. (A) General view of the four surface environments: wetland, grassland, localized mounds and amalgamated mounds. (B) Photograph showing the amalgamated mound where surface samples were collected and the seven sediment profile locations.

Analytical methods

Water analyses

Cations and anions were analysed using a Perkin-Elmer Optima 3300DV inductively coupled plasma – atomic emission spectrometer (Perkin-Elmer, Waltham, MA, USA) and a Dionex IC-3000 ion chromatograph (Dionex Corporation, Sunnyvale, CA, USA), respectively. Dissolved inorganic carbon (DIC) concentrations were determined using a Lachat IL550 TOC-TN analyzer (Hach Company, Loveland, CO, USA). Charge balances and saturation indices were determined from speciation calculations using PHREEQC with the LLNL database (Parkhurst & Appelo, 1999). Samples for stable carbon, hydrogen and oxygen isotope analyses of DIC and waters were submitted to the G.G. Hatch Stable Isotope Laboratory at The University of Ottawa.

X-ray diffraction

All sediment samples were dried at room temperature prior to analysis. Mineral phases in sediment samples were identified using powder X-ray diffraction (XRD) methods. Aliquots of sediment (2·0 g) were ground under anhydrous ethanol for 3 min using a McCrone micronizing mill and agate grinding elements. A 10 wt% internal standard of annealed CaF_2 was added to the samples to allow for quantification of amorphous content. Micronized samples were dried for *ca* 24 h and gently disaggregated with an agate mortar and pestle. Powder mounts were prepared against ground glass to minimize preferred orientation (Raudsepp & Pani, 2003). Quantitative phase analysis was conducted using Rietveld refinement of XRD data, which provides a measure of the weight-percent contribution of each mineral in a sample. All XRD data were collected using a Bruker D8 Focus Bragg-Brentano diffractometer (Bruker, Billerica, MA, USA) with a step size of 0·04° over a range of 3 to 80° 2θ at 0·8 sec per step. Iron monochromator foil, 0·6 mm divergence slit, incident and diffracted beam soller slits, and a Lynx Eye positive sensitive detector were used for collection of XRD data. A long fine focus Co X-ray tube was operated at 35 kV and 40 mA using a take-off angle of 6°. Search-match software by Bruker (DIFFRACplus EVA 14) was used for phase identification (Bruker AXS, 2008). Crystal structure data for Rietveld refinement were obtained from the International Centre for Diffraction Data PDF-4 + 2010. Rietveld refinement was completed using Topas Version 3 software (Bruker AXS, 2004). Wilson *et al.* (2009b) demonstrated that the Rietveld method can be used accurately to quantify hydrated Mg-carbonate minerals to a lower limit of *ca* 0·5 wt% under the operational conditions used in the laboratory.

Some samples showed broad peaks in their diffraction patterns that may be due to either poor crystallinity or variability in the chemical composition of the minerals. Compositional broadening occurs if there is a continuum of mineral compositions all giving slightly overlapping peaks. The result is broad peaks centred on the average composition of a number of chemically and structurally similar crystals. Crystallite size broadening is symptomatic of poorly crystalline materials, such as nano-scale carbonate crystals. The specific abundance determined for individual carbonate mineral phases in these sediments may have greater error due to the broadness of the peaks and uncertainty in Mg/(Mg + Ca) ratios.

Scanning electron microscopy

Scanning electron microscopy (SEM) of the sediment samples was performed at the Nanofabrication Facility at The University of Western Ontario. Samples were mounted onto aluminium stubs using 12 mm carbon adhesive tabs prior to being coated. A Filgen osmium plasma coater (OPC 80T) was used to apply a thin layer of osmium metal (5 nm) and a LEO 1540 XB field emission SEM (Zeiss, Oberkochen, Germany) was used to produce high-resolution images at an operating voltage of 1·0 kV. In addition, a quadrant backscatter detector was used for imaging at an operating voltage of 10 or 20 kV and an Oxford Instruments INCAx-sight energy dispersive spectrometer (EDS; Oxford Instruments, Abingdon, UK) was utilized for elemental analysis.

Aliquots (10 g) of sediment samples from profile 4 were reacted with 250 ml of 10% HCl over *ca* 24 h to remove nearly all the carbonate present in the sample; leaving only non-carbonate grains. The remaining material was filtered onto Whatman® 1 filter paper, air-dried at room temperature and examined using SEM.

Stable isotope analyses and radiocarbon dating

Samples of the seven sediment profiles were analysed for their stable carbon and oxygen isotopic compositions. Aliquots of sediment (30 to 50 mg) were placed in Labco exetainers and acidified using 85% H_3PO_4 at *ca* 72°C for 24 h to ensure complete reaction. The CO_2 generated was passed through an EtOH-dry ice cold trap,

subsequently mixed with *ca* 100 ml of laboratory air, and ultimately drawn into a Los Gatos Research (LGR®; Los Gatos Research, Mountain View, CA, USA) off-axis integrated cavity output laser spectrometer (Barker *et al.*, 2011). The LGR analyzer measures the absorption spectra of $^{12}C^{16}O^{16}O$, $^{13}C^{16}O^{16}O$ and $^{12}C^{16}O^{18}O$ in the near-infrared wavelength spectrum. The stable carbon and oxygen isotope values are reported in the conventional δ notation in per mil (‰) relative to Vienna Pee Dee Belemnite (VPDB) and Vienna Standard Mean Ocean Water (VSMOW), respectively. An in-house calcite standard with an accepted $δ^{13}C_{VPDB}$ value of $1·8 ± 0·2‰$ and $δ^{18}O_{VSMOW}$ value of $13·7 ± 0·3‰$ was measured at least every eight samples. The $δ^{18}O$ values of Mg-carbonate sediments were corrected for reaction with phosphoric acid using the fractionation values from Das Sharma *et al.* (2002). The fractionation factor for magnesite was used as a proxy for hydrated Mg-carbonate minerals.

Remnants of vegetation recovered from sediment profiles 6 and 7 were submitted to the Radiocarbon Dating Centre at the Australian National University, Canberra. Remnant vegetation samples were pre-treated with an acid/base/acid treatment that altered between 1 M HCl and 1 M NaOH in 30 min batches until wash solutions were clear. A final 1 h acid wash was performed. Samples were rinsed with Milli-Q™ (Millipore, Billerica, MA, USA) water until neutral and dried overnight. A standard procedure for sample combustion and CO_2 purification was conducted and followed by graphitization using the method of Santos *et al.* (2004). Carbon-14 analyses were performed using a single-stage accelerator mass spectrometer (Fallon *et al.*, 2010; Beavan *et al.*, 2012).

RESULTS

## Hydrogeochemistry and stable isotopic composition of waters

Hydrogeochemical data and saturation indices for relevant carbonate minerals are summarized in Table 2. The spring water, collected *ca* 3·5 km from the playas, had a pH of 8·00, Mg concentration of 70 mg l^{-1} and alkalinity of 400 mg HCO$_3^-$ l^{-1}. The well, *ca* 50 m from the playa, had a pH of 8·14, Mg concentration of 474 mg l^{-1} (Mg/Ca = 107) and alkalinity of 2610 mg HCO$_3^-$ l^{-1}. A sample from the water table was collected while augering in the amalgamated mound and had a pH of 7·98, Mg

Table 2. Water chemistry of the south-eastern playa near Atlin, British Columbia. Analytes not detected are listed as 'n.d.' PHREEQC (Parkhurst & Appelo, 1999) was used to calculate saturation indices for relevant mineral phases including lansfordite (lns), nesquehonite (nsq), hydromagnesite (hmg), magnesite (mgs), huntite (hun), disordered dolomite (dol-dis), ordered dolomite (dol-ord), aragonite (ara) and calcite (cal).

Sample location	pH	Alkalinity (mg HCO$_3^-$ l^{-1})	Cation concentrations (mg l^{-1})							Anion concentrations (mg l^{-1})			
			Mg	Ca	Si	Na	K	Fe	Al	SO$_4$	Cl	NO$_3$	PO$_4$
Spring	8·00	400	70·0	48·0	4·9	3·6	1·1	n.d.	0·24	8·0	2·6	1·0	n.d.
Groundwater well	8·14	2610	474	7·3	11·5	16·1	6·8	0·07	0·16	39·8	1·9	0·1	n.d.
Mound water (profile 4 location)	7·98	8480	1550	2·1	16·7	87·4	14·3	0·22	0·25	77·4	7·4	4·1	n.d.
Isolated pond	7·54	5150	800	68·1	43·7	64·8	9·2	0·28	0·24	57·9	3·3	n.d.	n.d.
Wetland (north lobe)	8·61	4780	887	9·9	31·1	57·5	11·0	0·15	0·26	97·0	16·6	n.d.	n.d.
Wetland (south lobe)	8·56	4720	865	9·2	33·8	76·1	12·4	0·04	0·26	80·5	6·4	n.d.	n.d.

Sample location	Saturation indices								
	Lns	Nsq	Hmg	Mgs	Hun	Dol-dis	Dol-ord	Ara	Cal
Spring	−1·83	−2·79	−8·24	0·32	−0·16	0·94	2·61	0·41	0·55
Groundwater well	−0·32	−1·50	−2·29	1·69	3·65	2·06	3·76	0·16	0·31
Mound water (profile 4 location)	0·27	−0·68	1·08	2·43	5·51	2·41	4·07	−0·24	−0·09
Isolated pond	−0·51	−1·47	−3·13	1·64	4·19	2·65	4·31	0·79	0·94
Wetland (north lobe)	0·46	−0·49	2·93	2·62	7·17	3·68	5·34	0·85	1·00
Wetland (south lobe)	0·41	−0·54	2·63	2·57	6·95	3·56	5·23	0·78	0·93
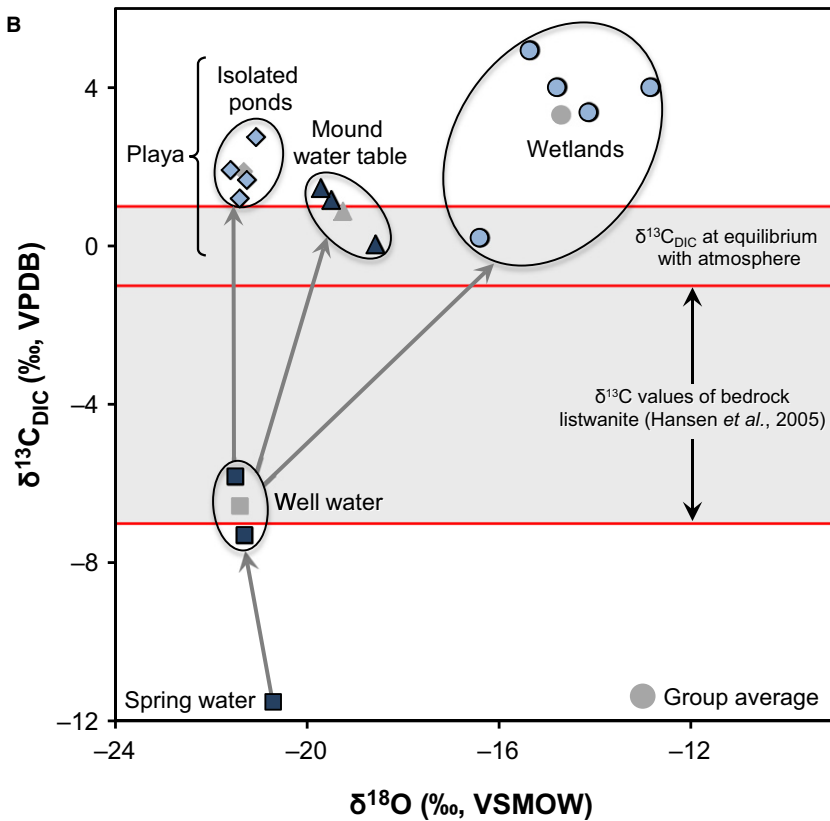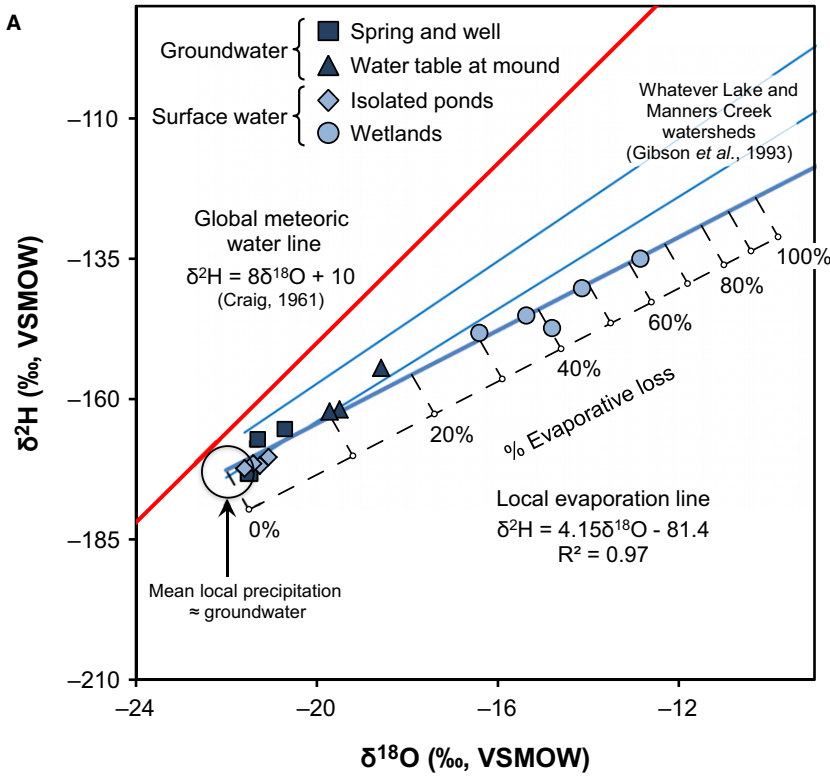
Fig. 3. (A) Plot of δ^2H and $\delta^{18}O$ values of the water samples collected from the Atlin site. Samples are grouped based on the water source. The global meteoric water line by Craig (1961) is plotted in the absence of a local meteoric water line. Isotopic data were used to define a local evaporation line (LEL) for the catchment and to estimate evaporation losses as a percentage of input. The LELs for two watersheds in northern Canada by Gibson *et al.* (1993) are shown for comparison. (B) Plot of $\delta^{13}C_{DIC}$ and $\delta^{18}O$ values of the water samples collected from the Atlin site including water source group averages.

concentration of 1550 mg l^{-1} (Mg/Ca = 1215) and much greater alkalinity than the aforementioned samples, at 8483 mg HCO$_3^-$ l^{-1}.

The north and south lobes of the main wetland had similar pH (8·61 and 8·56), Mg concentrations (887 mg l^{-1} and 865 mg l^{-1}; average Mg/Ca = 151) and alkalinities (4780 mg HCO$_3^-$ l^{-1} and 4720 mg HCO$_3^-$ l^{-1}). The main wetland had a cation composition of Mg >> Na > Si > K > Ca with the Mg concentration being nearly balanced by alkalinity (Mg/alkalinity = 0·95). The Mg/Ca molar ratios of waters in the playa were typically in the order of at least 100 : 1 and were as high as >1000 : 1. The isolated ponds generally had lower pH values (for example, 7·54) and greater Ca concentrations, for instance, 68 mg l^{-1} compared to 9 mg l^{-1} in the main wetland.

A plot of δ^{2}H and δ^{18}O values for all water samples defines a local evaporation line (LEL) in Fig. 3A. The LEL is described by the equation δ^{2}H = 4·15δ^{18}O−81·4. The percent evaporative loss was calculated using δ^{18}O isotope data as described by Gibson *et al.* (1993). Because there is no evaporation from an open water body when it is ice covered, calculations of evaporative losses assumed mean relative humidity and temperature from April to October when the average daily temperature was above 0°C. For this period, the average relative humidity recorded at Dease Lake, British Columbia, Canada, was 53%, which is the closest weather station (*ca* 250 km from Atlin) that records atmospheric humidity data. The isotopic composition of atmospheric water vapour was assumed to be in equilibrium with the mean annual precipitation.

The δ^{13}C$_{DIC}$ and δ^{18}O values for water samples are used to trace the geochemical evolution of waters in the Atlin region (Fig. 3B). Isotope values are listed in Table S3. The spring and well waters had δ^{18}O values in the range of −21 to −22‰. Water from the well (δ^{13}C$_{DIC}$ ≈ −6·5‰) was significantly enriched in ^{13}C by *ca* +5‰ relative to the spring water (δ^{13}C$_{DIC}$ ≈ −11·5‰). Mound water table samples were enriched in both ^{13}C and ^{18}O by *ca* +7‰ and +2‰ compared to the well water, respectively. The isotopic compositions of samples from the isolated ponds clustered in a narrow range of δ^{13}C$_{DIC}$ and δ^{18}O values with averages of 1·9‰ and −21·3‰, respectively. There was greater variation in isotopic compositions of the main wetland samples from the south-eastern playa, with δ^{18}O ranging from −16 to −13‰ and δ^{13}C$_{DIC}$ ranging from 0 to 5‰.

## Sediment deposition in the wetlands and grasslands

Nesquehonite films on water surfaces (Fig. 4A) and crusts on exposed surfaces around the wetland periphery were observed and have previously been documented (Power *et al.*, 2007, 2009). In the south lobe of the main wetland, benthic microbial mats dominated by cyanobacteria lined the wetland floor and contained dypingite and aragonite (Power *et al.*, 2007, 2009). Carbonate accumulation within wetlands has been observed to cause progressive infilling of features. For instance, a plastic lid (60 × 45 cm) was placed in the wetland for two years, during which time a *ca* 3 cm thick microbial mat with carbonate sediment formed on the lid (Fig. 4B). Below the benthic mats were black, anoxic sediments composed primarily of aragonite (Power *et al.*, 2009). Lithified and consolidated aragonite sediments stained by iron oxyhydroxides were present in some areas along the periphery of the wetland (Fig. 4C). In some instances, pisolites with inverse-graded bedding were noted (Power *et al.*, 2009).

Tufts of grasses, fortified by carbonate sediments, resembled 'islands' within the main wetland (Fig. 4D). These structures were typically less than 1 m in diameter and were able to support the weight of a person. Small isolated portions of wetland (Fig. 4E) were scattered within the grassland areas. The density of grasses varied from fully covering the ground surface to being sparsely distributed amongst carbonate sediments (Fig. 4E).

Interspersed in the grassland area were localized mounds that were semi-circular with distinct boundaries, metre-scale in diameter, and tens of centimetres above lower lying grasses (Fig. 4F). In some cases, consolidated aragonite rubble was found amongst localized mounds.

Sediment deposition in the amalgamated mounds

X-ray diffraction analyses of sediments coupled with field observations and electron microscopy provided a comprehensive understanding of the composition of the Atlin playas. Surface samples are summarized first (Figs 5 to 7), followed by the seven sediment profiles (Fig. 8). Sediment profiles are shown in a simplified cross-sectional view in Fig. 9, which depicts three sedimentary units: Mg-carbonate sediments, Ca–Mg-carbonate sediments and siliciclastic mud.
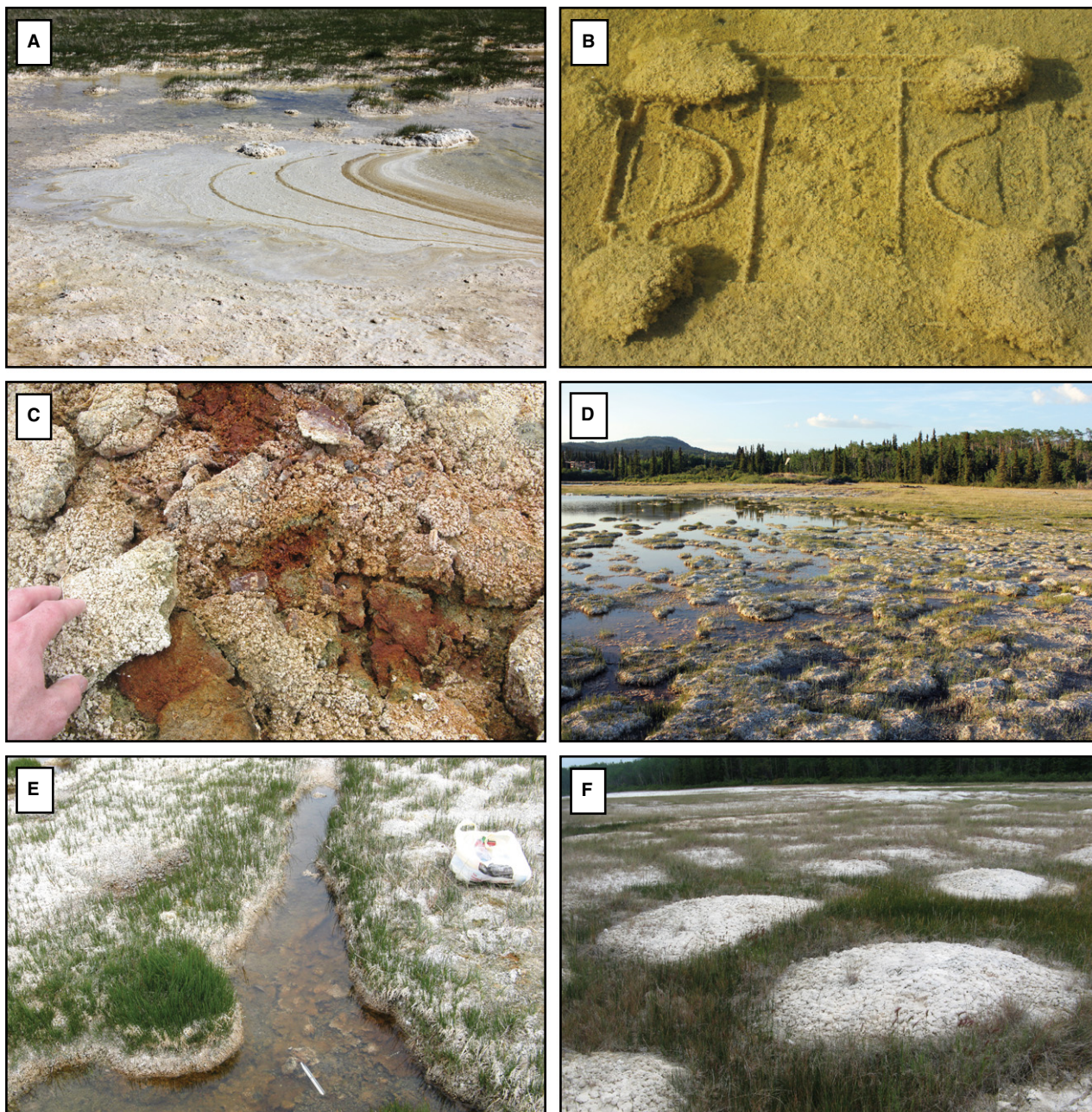
Fig. 4. Photographs from the south-eastern playa. (A) A nesquehonite film on the surface of the south lobe of the main wetland. Bottom of photograph is *ca* 2 m wide. (B) A plastic lid (60 × 45 cm) below the water surface covered by benthic mats and carbonate sediment after two years of being in place. (C) Consolidated aragonite stained by iron hydroxides along the periphery of the north lobe of the main wetland. (D) South edge of the main wetland showing tufts of grass forming 'islands' in the wetland. Bottom of photograph is *ca* 3 m wide. (E) An isolated portion of wetland; note the variability in grass density. (F) Numerous localized mounds (metre-scale) of hydromagnesite amongst grasses.

Surface field observations and mineralogy

Localized and amalgamated mounds gave the playas a hummocky surface topography. The surface appearance of the mounds was fairly uniform, consisting of white carbonate mud (Fig. 5A). In some cases, sediments were slightly grey or brown, probably indicating the presence of organic matter. The higher area of the amalgamated mound was covered by extensive desiccation cracks that created a cauliflower-like texture, whereas polygonal desiccation cracks were more common in lower lying areas (Fig. 6A).
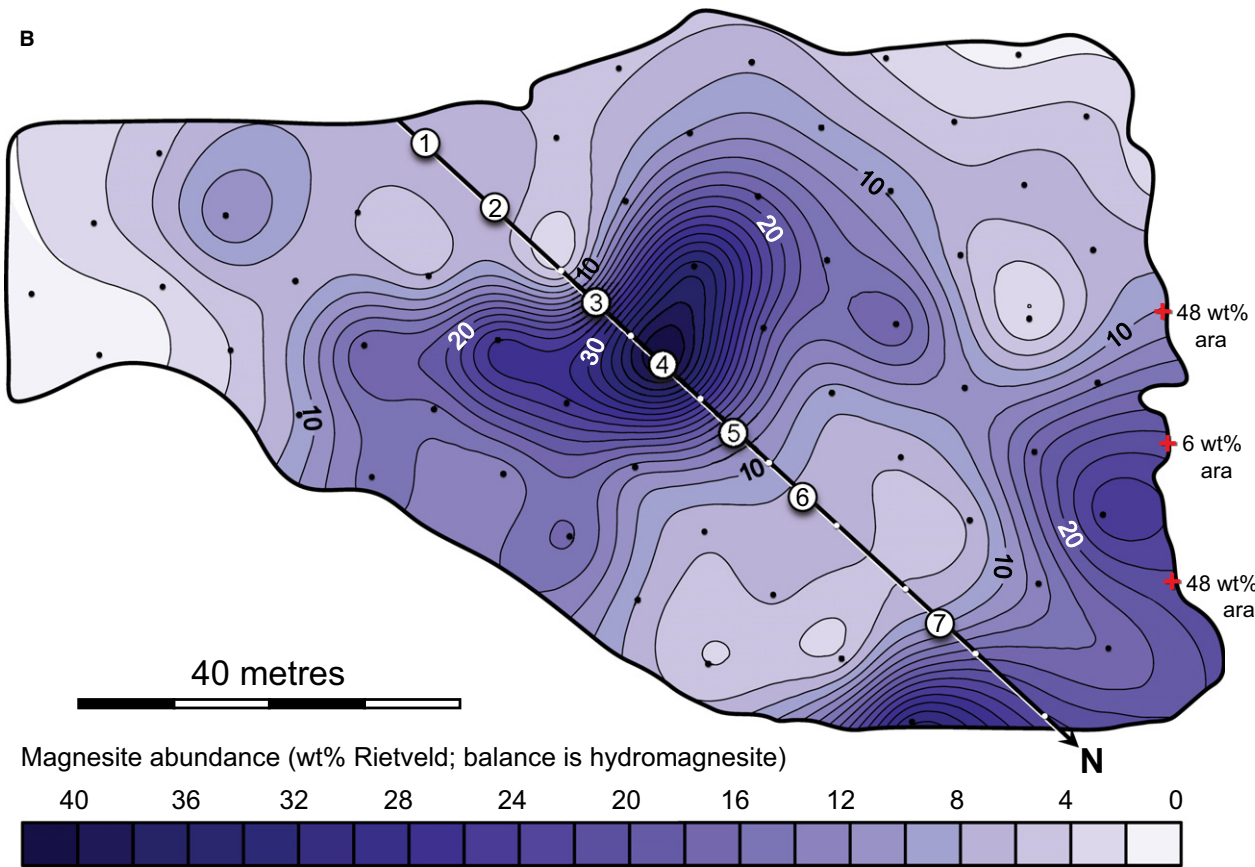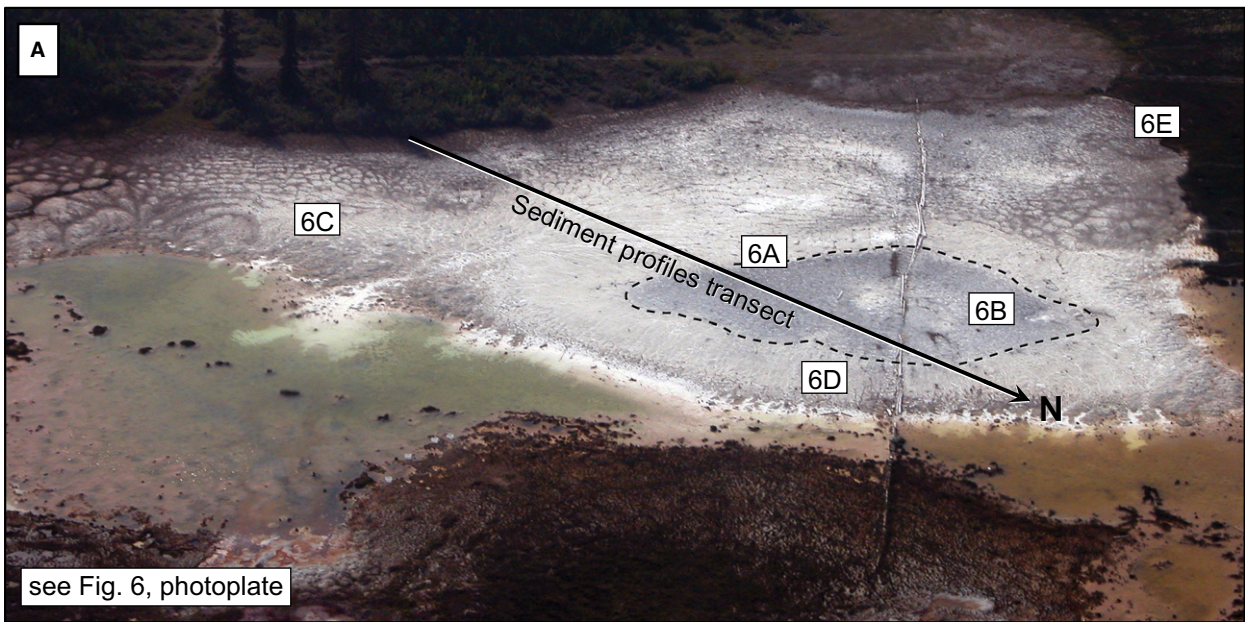
Fig. 5. (A) Aerial photograph of the amalgamated mound from which 66 surface samples were collected in a 10 m incremented grid. The locations of photographs in Fig. 6 are shown. Transect is 75 m long. (B) Magnesite abundance (balance is hydromagnesite) of the surface sediments; dots indicate sampling locations. Note that the three samples that contained aragonite near the edge of the mound were excluded in the contour map.
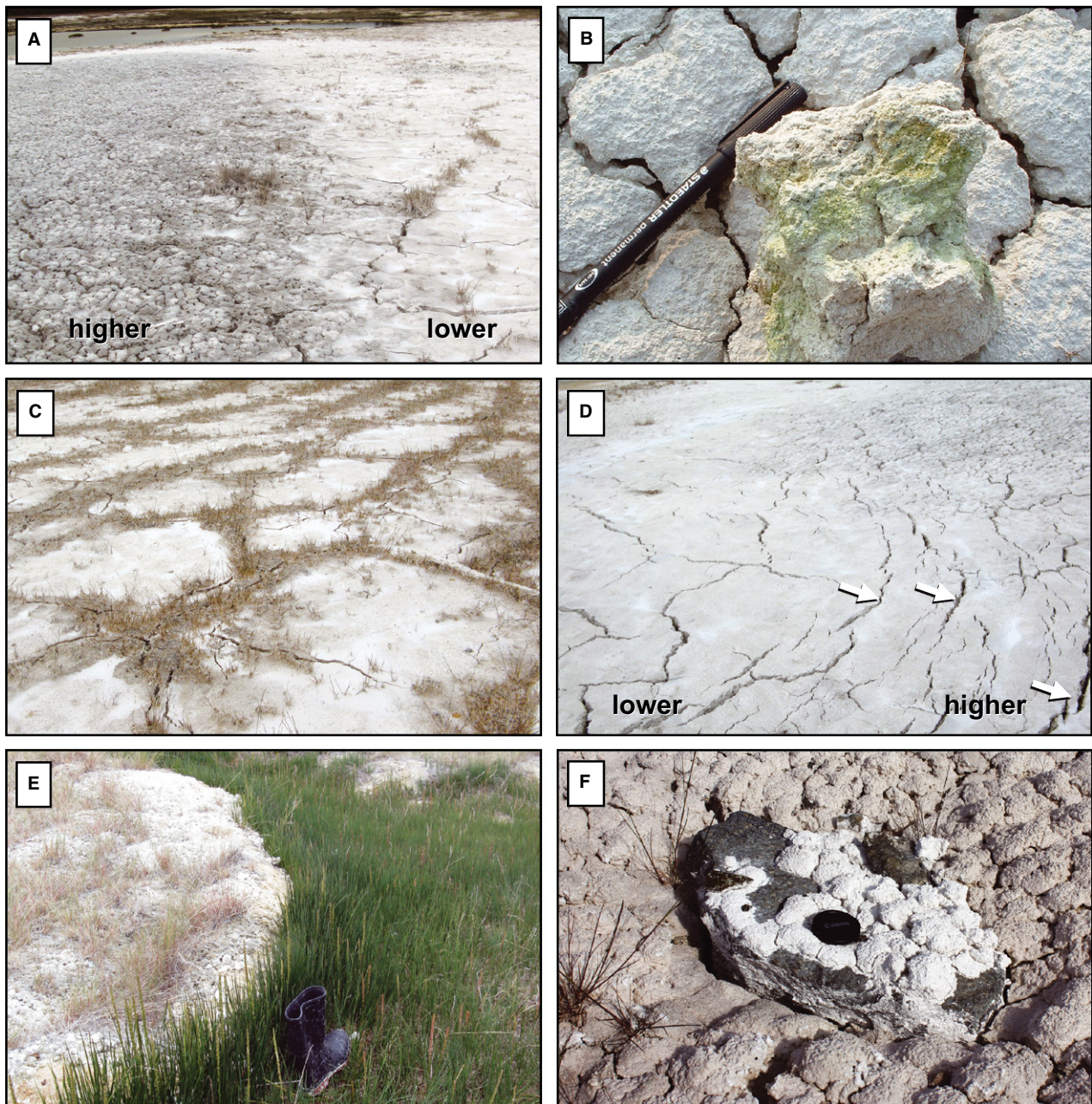
Fig. 6. Photographs of the amalgamated mound; locations are marked on the aerial photograph in Fig. 5A. (A) Cauliflower desiccation cracking on the left and polygonal desiccation cracking on the right, slightly downslope. Bottom of photograph is *ca* 3 m wide. (B) A piece of Mg-carbonate sediment, removed from the surface and placed on its side, showing colonization of cyanobacteria (green) on the crack walls; note the cauliflower texture of the surface. Marker is 14 cm long. (C) Polygonal cracking of Mg-carbonate sediments located near the edge of the amalgamated mound that have been colonized by grasses. Bottom of photograph is *ca* 1 m wide. (D) Transverse cracks on the slope of an amalgamated mound; downslope is to the left. Bottom of photograph is *ca* 2 m wide. (E) Western edge of the amalgamated mound being *ca* 30 cm above grasses to the right of the image (boot for scale is *ca* 40 cm tall). (F) Serpentinite stone partially covered in hydromagnesite (lens cover for scale is 6 cm wide); note that the stone sits on top of Mg-carbonate sediments.

Cyanobacteria were commonly found colonizing the edges of desiccation cracks (Fig. 6B). Modest colonization by grasses was typically observed towards the edge of the playas, in some cases following the pattern of desiccation cracks (Fig. 6C). Transverse cracks were observed on the east-fac-

ing slope of the amalgamated mound (Fig. 6D). The north-west edge of this amalgamated mound was very distinct with a drop of *ca* 30 cm from the Mg-carbonate sediments to a grass covered surface (Fig. 6E). In some locations, particularly in the northern and south-western playas, there were stones, typically of serpentinite, that rested on top of Mg-carbonate sediments at the surface of the playa (Fig. 6F).

The surface sediments were predominately composed of hydromagnesite (59 to 99 wt%) with the remainder being magnesite (1 to 41 wt%) as determined using Rietveld refinement of XRD data (Fig. 5B). This uppermost unit consisting of only Mg-carbonate minerals is henceforth referred to as 'Mg-carbonate sediments'. There were two magnesite-rich zones; one near the middle of the mound with a somewhat west–east trend and a second near the north edge of the mound. Three samples at the very north-west edge of the mound contained 48 wt%, 6 wt% and 48 wt% aragonite and were excluded from the magnesite abundance contour plot.

Scanning electron microscope micrographs of near-surface sediments showed that hydromagnesite typically existed as stacks of individual plates. Plates were submicron to a few microns wide and *ca* 100 nm thick (Fig. 7A). Magnesite was present as either individual crystals or aggregates of crystals. The size of these aggregates ranged from submicron to several microns (Fig. 7B). The characteristic rhombohedral shape of the magnesite crystals was usually only observed in a portion of these aggregates (arrows in Fig. 7B). Magnesite crystals were closely associated with hydromagnesite and were seen wedged between hydromagnesite plates (Fig. 7C).

Magnesium-carbonate sediments

As previously mentioned, the top unit consisted of predominately hydromagnesite and magnesite (Figs 8 and 9). Sediment profiles 1 and 2, located near the outer edge of the playa, reached depths of 60 cm and 110 cm, respectively, and did not intersect the water table. Profiles 3 to 7 reached depths of between 220 cm and 420 cm below the ground surface and intersected the water table at depths of *ca* 80 to 120 cm. Sediment profile 6 was located at the high point of the mound and profile 7 was located downslope towards the north lobe of the main wetland.

The locations of profiles 3, 4 and 5 correspond to one of the magnesite-rich zones identified in the magnesite contour plot (Fig. 5B). Surface magnesite abundances in profiles 3, 4 and 5
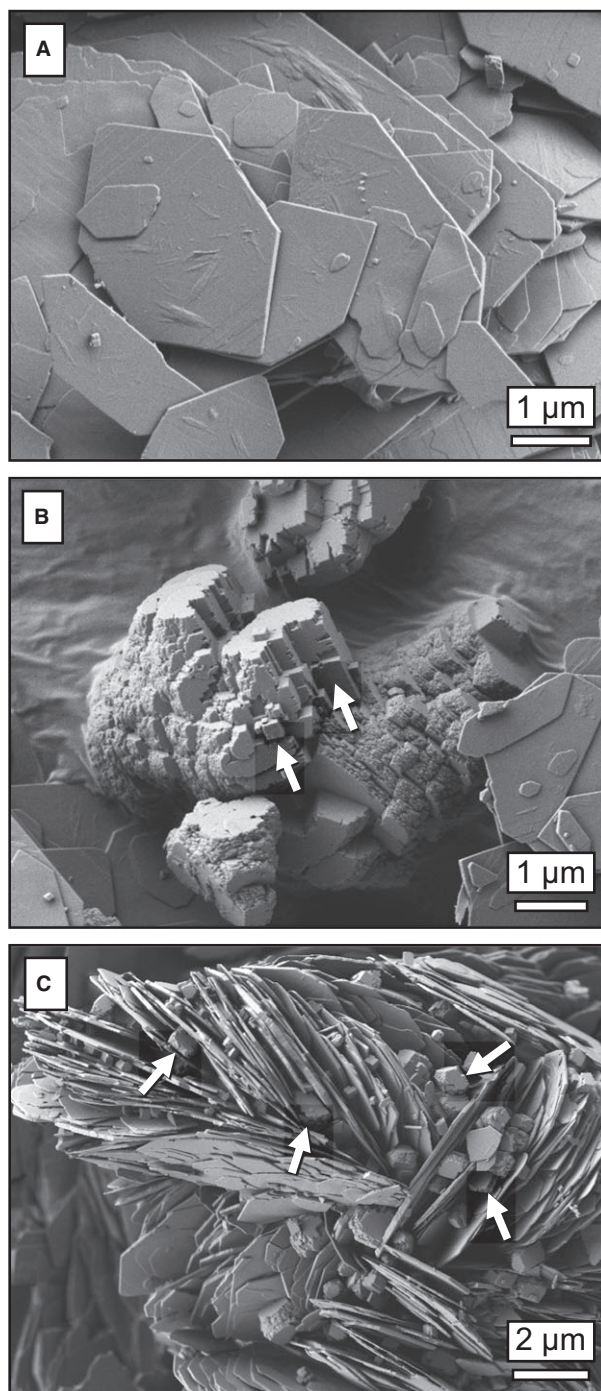
Fig. 7. Representative scanning electron micrographs of carbonate minerals from sediment profile 4. (A) Typical appearance of stacked hydromagnesite plates. (B) A large (several micron) aggregate of magnesite with characteristic rhombohedral shape (arrows). (C) An aggregate of hydromagnesite plates with numerous magnesite crystals (arrows) wedged between plates.

were 20 wt%, 41 wt% and 13 wt%, respectively, with the remainder being hydromagnesite. In the other profiles, magnesite abundance
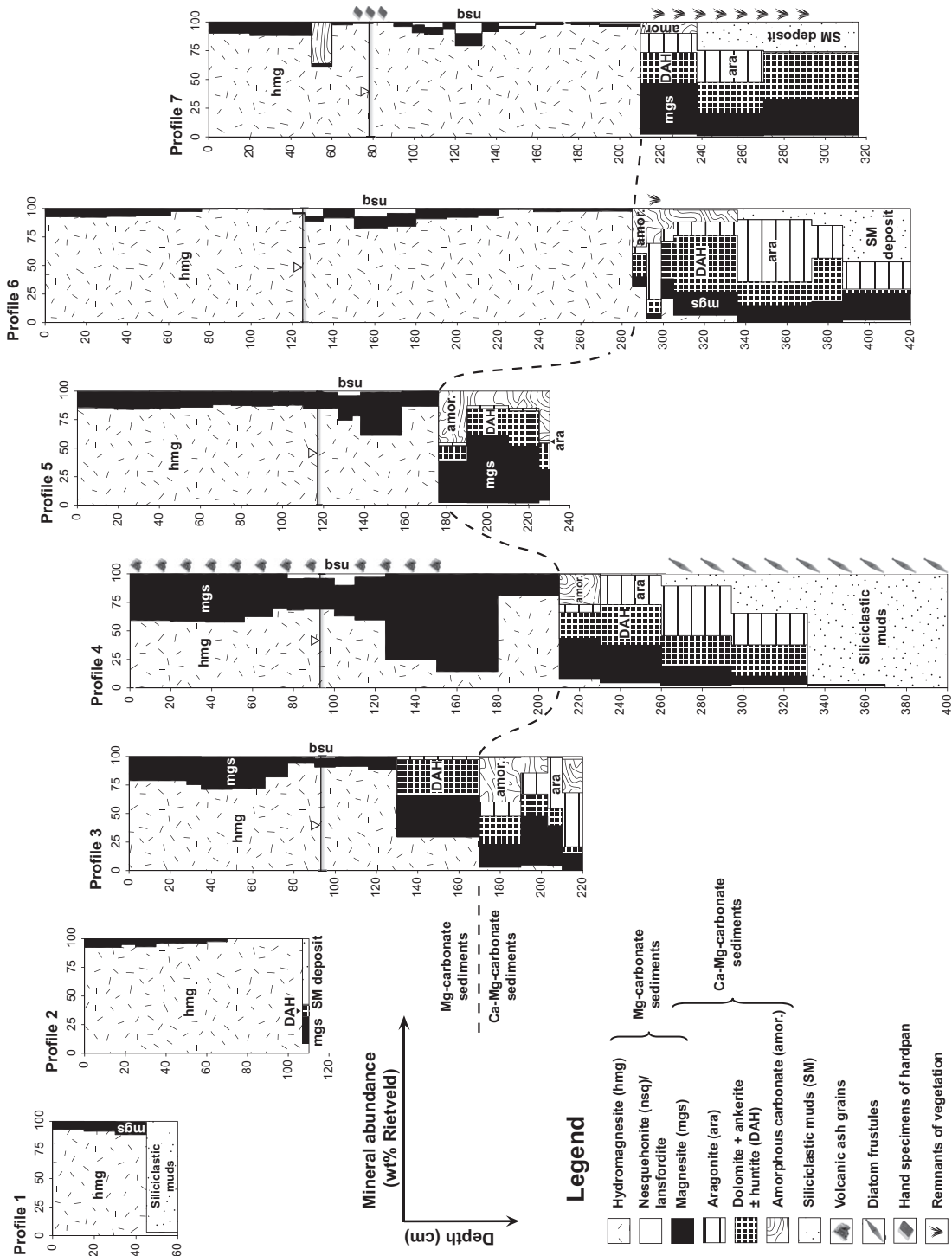
Fig. 8. Mineral abundances (x-axis in wt%) of the playa sediments collected with depth (y-axis in cm). The minerals plotted include hydromagnesite (hmg), magnesite (mgs), nesquehonite (nsq), aragonite (ara), and dolomite, ankerite and huntite (grouped together as DAH), and silicate minerals grouped together as siliciclastic muds. Locations at which particles of volcanic ash and diatom frustules were observed (profile 4) and hand specimens of the lansfordite hardpan (profile 7) and remnant vegetation (profiles 6 and 7) were collected are indicated symbolically. The sediment profiles are positioned vertically based on their relative elevations.
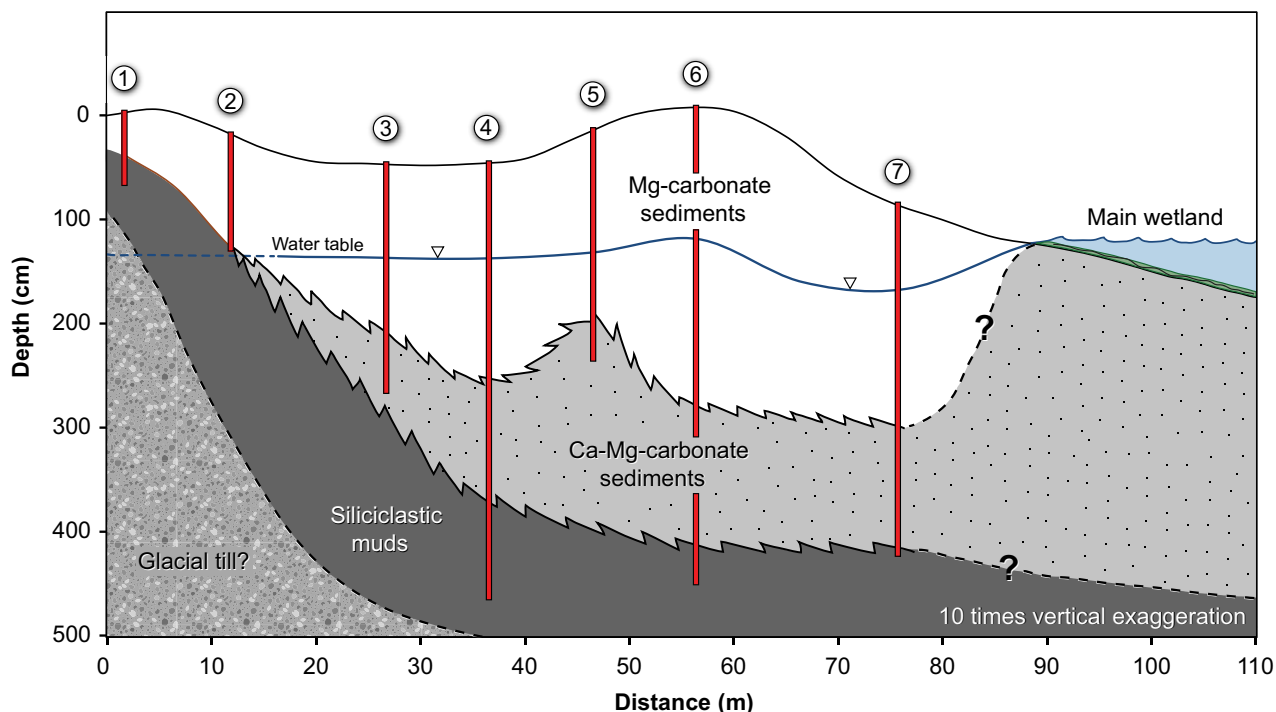
Fig. 9. A cross-sectional schematic along the sediment profile transect showing the locations and depths of the seven sediment profiles. The position of the water table is highlighted along with the three major sediment units: Mg-carbonate sediments, Ca–Mg-carbonate sediments and siliciclastic muds. Solid lines are based on data, whereas dashed lines are interpretations.

at the surface was 7 to 10 wt%. Sediment textures changed with depth from clay-like to crumbly, with hard nodules being observed within sediments near the water table. Magnesite abundance remained relatively constant, or else increased slightly up to depths of *ca* 60 cm; however, magnesite abundances decreased notably in the vicinity of the water table.

Partially cemented sediments forming a hardpan were found near the water table. A small pit was dug near the location of profile 7 to obtain hand specimens (up to 15 × 10 cm and 4 cm thick) of the hardpan. The hardpan was brittle enough to be broken and crumbled by hand. It had a similar colouration, white with a slight yellow tinge, as the surrounding sediments. Transparent millimetre-scale crystals of presumably lansfordite were visible on freshly exposed surfaces of the hardpan. A hardpan was also observed while augering in the northern playa and in a separate location in the southeastern playa. X-ray diffraction analyses of hand specimens were performed within two weeks after collection and on average (*n* = 3) were composed of hydromagnesite (57 wt%), lansfordite (36 wt%), magnesite (4 wt%) and nesqueho-

nite (3 wt%). Lansfordite was absent in profile samples, yet up to 10 wt% of nesquehonite in sediments was detected near the water table. Importantly, profile samples were stored at room temperature for more than one year prior to analysis. It is presumed that the presence of nesquehonite resulted from dehydration of lansfordite postsampling. This assumption is consistent with the reported stability of lansfordite; at >10°C lansfordite will dehydrate to form nesquehonite (Ming & Franklin, 1985; Königsberger *et al.*, 1999).

Below the water table, sediments remained a mixture of hydromagnesite and magnesite with abundance of the latter generally increasing with depth in profiles 3, 4 and 5. In profile 4, magnesite abundance increased to 86 wt% at a depth of 150 to 180 cm (Fig. 8). In profiles 3 and 5, the maximum magnesite abundance measured was 37 wt% and 38 wt% in the Mg-carbonate sediments, respectively. In profiles 6 and 7 below the water table, the amount of magnesite increased before decreasing at greater depths.

Scanning electron microscopy of acid-treated samples from profile 4 revealed the presence of volcanic ash particles from the surface to *ca* 1·5 m depth. Many particles appeared unweath-

ered, with dish-shaped depressions and vesicles being visible (Fig. S1A to C). Energy dispersive spectrometer data were used to obtain semi-quantitative estimates of the elemental abundance for Si, Na and K, which were converted to SiO_2, Na_2O and K_2O, respectively (see Fig. S1D and E). Based on this analysis, the ash particles had a rhyolitic composition.

Calcium–Magnesium-carbonate sediments
In profiles 3 to 7, at depths well below the water table, there was a distinct change in the appearance and mineralogical composition of the sediments (Fig. 8). The abundance of hydromagnesite substantially decreased, yet magnesite abundance remained relatively high. Calcium-bearing carbonate phases including aragonite, dolomite, ankerite and possibly huntite were present. The XRD patterns of these sediments had broad peaks, suggesting poor crystallinity and/or variable Mg/(Mg + Ca) ratios of some carbonate phases (Nash *et al.*, 2011). For simplicity, the abundance of dolomite, ankerite and huntite is grouped together and listed as 'DAH' in Fig. 8. The amorphous content in the Ca–Mg-carbonate sediment samples was up to *ca* 40 wt % and was assumed to be carbonate because samples with amorphous content would nearly completely dissolve when tested with dilute acid. Amorphous carbonate was typically greatest near the transition between the Mg-carbonate sediments and these sediments containing Ca-bearing carbonate phases. Sediments containing magnesite, aragonite, DAH carbonate minerals and amorphous carbonate are henceforth referred to as 'Ca–Mg-carbonate sediments'. Minor amounts of hydromagnesite were noted near the base of some profiles. The minor hydromagnesite was probably contamination incurred during augering, wherein shallower sediments are caught in the auger as a result of holes narrowing under the weight of overlying sediments.

Remnants of vegetation were observed in sediment profiles 6 and 7 at depths of 292 to 299 cm and 215 to 290 cm, respectively (Fig. 8). The abundance was considerably greater in pro-file 7 and appeared to increase to a depth of 290 cm, yet was absent at greater depths. This buried vegetation resembled modern grass roots found in the playas. Remnant vegetation from profile 6 (292 to 299 cm depth) and profile 7 (238 to 247 cm depth) had $\delta^{13}C$ values of $-22\cdot2 \pm 5\cdot6\permil$ and of $-22\cdot7 \pm 1\cdot2\permil$, respectively. The age of remnant vegetation was 8045 ± 257 cal yr BP in profile 6 and 6527 ± 114 cal yr BP in profile 7, based on radiocarbon analysis. Data of the remnant vegetation are summarized in Table 3.

Siliciclastic muds
Magnesium-carbonate sediments were found to overlay a dark grey to black siliciclastic mud at the location of profile 1. There was a relatively sharp boundary between these units. The siliciclastic mud (depth >45 cm) was comprised of quartz (38 wt%), albite (29 wt%), orthoclase (12 wt%), clinochlore (10 wt%), tremolite (5 wt%), diopside (3 wt%), hydromagnesite (3 wt%) and trace lizardite (Fig. 8). For simplicity, silicate minerals are grouped together in Fig. 8. Silicate minerals were also found near the base of profile 2 (depth >107 cm). However, the base of profile 2 differed from profile 1 with the presence of Ca-bearing carbonate phases, mainly dolomite (14·5 wt%).

Siliciclastic mud was found underlying the Ca–Mg-carbonate sediments in profiles 4, 6 and 7. In profile 4, the abundance of silicate minerals increased from *ca* 260 to 370 cm; at depths >370 cm the sediments were entirely composed of silicate minerals. The abundance of magnesite decreased over the same interval. At 400 cm depth, the mud contained quartz (32 wt%), orthoclase (26 wt%), albite (17 wt%), clinochlore (12 wt%), tremolite (8 wt%), lizardite (3 wt%) and diopside (2 wt%) (Fig. 8). The mineralogical composition, appearance and texture of this siliciclastic mud were similar to what was observed at the base of profile 1. Profiles 6 and 7 also contained high abundances of silicate minerals near their bases; sediments composed only of silicate minerals were not reached. Although absent in

Table 3. Stable and radiogenic carbon isotopes of buried vegetation from profiles 6 and 7.

Sample	$\delta^{13}C$	Percent modern carbon (pMC)	^{14}C age	Calibrated calendar age (BP)	
Profile 6	$-22\cdot2 \pm 5\cdot6$	$40\cdot8 \pm 0\cdot5$	7190 ± 110	8161–7934 (68·2%)	8302–7788 (95·4%)
Profile 7	$-22\cdot7 \pm 1\cdot2$	$49\cdot0 \pm 0\cdot3$	5735 ± 45	6629–6471 (68·2%)	6641–6413 (95·4%)

Fig. 10. Plots of $\delta^{18}O$ (A) and $\delta^{13}C$ (B) values versus depth (cm) of bulk carbonate sediments from sediment profiles. The position of the water table (dashed line) was used as a datum (depth = 0 cm) with Mg-carbonate samples from profiles 2 to 7 plotted as depth from the water table. Profile 2 was plotted assuming an approximate water table of 120 cm depth; profile 1 was omitted. Ca–Mg-carbonate sediments were plotted in relation to the deepest Ca–Mg-carbonate boundary (i.e. −163 cm from the water table; dashed-dotted line). Ca–Mg-carbonate sediments (solid squares), Mg-carbonate sediments (open diamonds) and samples of the lansfordite hardpan (triangles) are plotted. Plots of $\delta^{18}O$ (C) and $\delta^{13}C$ (D) values of bulk carbonate sediments from grassland sediments with depth (cm). Mg-carbonate sediments (mainly hydromagnesite; open squares) and Ca–Mg-carbonate sediments (mainly aragonite and ankerite; solid squares) are plotted using data from Power *et al.* (2009). Measurement error is smaller than the symbols employed.
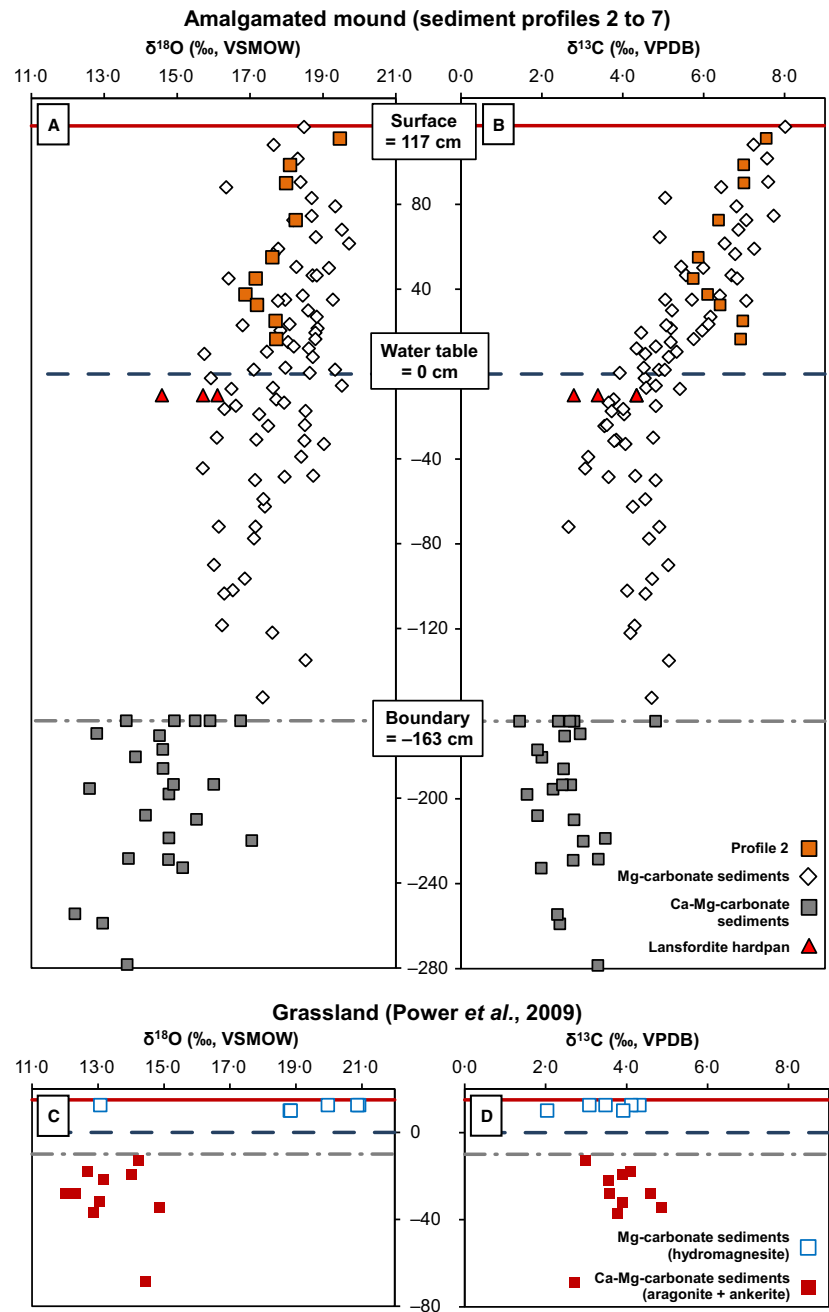
the overlying Mg-carbonate sediments, diatom frustules (Fig. S2A to C) of at least three species were present in the Ca–Mg-carbonate sediments at 270 cm depth to the siliciclastic mud at a depth of 400 cm in sediment profile 4.

Stable carbon and oxygen isotopes of carbonate sediments

The $\delta^{18}O$ and $\delta^{13}C$ values of the bulk carbonate sediments collected from sediment profiles are

plotted in Fig. 10A and B. In order to directly compare data from profiles 2 to 7, the water table was used as a datum with its depth set to 0 cm. Because profile 2 did not intersect the water table, it was plotted based on the water table depth in relation to profile 3; profile 1 was omitted. The $\delta^{18}O$ and $\delta^{13}C$ values of the Mg-carbonate sediments were plotted with distance from the water table. Profile 6 had a ground surface and Ca–Mg-carbonate boundary with the greatest distances of +117 cm and −163 cm from

the water table (Fig. 10A and B). The $\delta^{18}O$ and $\delta^{13}C$ values of the Ca–Mg-carbonate sediments were plotted in relation to the −163 cm depth (Fig. 10A and B). The Ca–Mg-carbonate sediments had $\delta^{18}O$ values ranging from 12·2 to 17·1‰ (average = 14·6‰) and $\delta^{13}C$ values ranging from 1·5 to 3·6‰ (average = 2·6‰). The Mg-carbonate sediments above the Ca–Mg-carbonate boundary were enriched by an average of +1·6‰ in ^{18}O and +1·9‰ in ^{13}C relative to the Ca–Mg-carbonate sediments immediately below the boundary. Mg-carbonate sediments had $\delta^{18}O$ and $\delta^{13}C$ values that ranged from 15·7 to 19·7‰ (average = 17·8‰) and 2·7 to 8·0‰ (average = 5·2‰), respectively. Average $\delta^{18}O$ values increased by *ca* +1‰ from the Ca–Mg-carbonate sediment boundary to the surface. $\delta^{13}C$ values of the Mg-carbonate sediments were most depleted at *ca* 20 cm below the water table. $\delta^{13}C$ values increased linearly from the water table towards the ground surface, reaching values of *ca* 8‰. The average $\delta^{18}O$ and $\delta^{13}C$ values of the hardpan were 15·5‰ and 4·0‰, respectively. The $\delta^{13}C$ values of profile 2 were the lowest at *ca* 50 cm above the modern water table.

In order to relate the sediment samples to the Atlin waters, stable isotopic compositions of carbonate sediments were converted to equivalent $\delta^{18}O$ values of water and $\delta^{13}C$ values of DIC based on equilibrium fractionation. These data are plotted in Fig. 11 and listed in Table S1. Fractionation factors at 10°C for hydrated Mg-carbonate minerals (hydromagnesite + nesquehonite + lansfordite; O'Neil & Barnes, 1971; Wilson *et al.*, 2010) and magnesite (Romanek *et al.*, 1992; Deines, 2004) were used, whereas fractionation factors at 25°C for dolomite (+ ankerite + huntite; DAH + amorphous carbonate; Ohmoto & Rye, 1979; Vasconcelos *et al.*, 2005; Zheng, 1999) and aragonite (Romanek *et al.*, 1992; Kim *et al.*, 2007) were used. Because the stable carbon equilibrium fractionation factor for the hydrated Mg-carbonate minerals at 10°C is not known, the fractionation factor for dypingite at 25°C as determined by Wilson *et al.* (2010) was used as a substitute, assuming the same temperature dependency for magnesite. Temperatures in the wetland during the summer months may be close to 25°C (Power *et al.*, 2007), whereas temperatures from the water table to the ground surface as measured during sediment sampling were 6 to 14°C. As such, a warmer temperature was chosen for aragonite and dolomite that were more closely associated with a wetland environment and a cooler temperature for hydro-

magnesite and magnesite because these minerals were most common in the mounds. In the case of sediment samples with mixed mineralogies (for example, hydromagnesite + magnesite), weighted averages for fractionation factors were based on the molar ratios of carbon and oxygen for the mineral constituents. Equilibrium fractionation factors with references are listed in Table S2. Assuming equilibrium fractionation, Ca–Mg-carbonate sediments precipitated from waters with stable carbon and oxygen isotopic compositions that ranged from approximately the average well water ($\delta^{18}O = -21\cdot4‰$ and $\delta^{13}C = -6\cdot6‰$) to $\delta^{18}O$ values of up to −15‰ and $\delta^{13}C$ values up to −1·2‰ (Fig. 11A). Isotopic values of the Mg-carbonate sediments clustered with $\delta^{18}O$ values of between −19‰ and −15‰ and $\delta^{13}C$ values of between −4‰ and 2‰ (Fig. 11B). Two outlying samples (average $\delta^{18}O = -20\cdot1‰$ and average $\delta^{13}C = -6\cdot1‰$) correspond to the two samples with the greatest magnesite abundances from profile 4 (125 to 180 cm; Fig. 8). The lansfordite hardpan ($n = 3$) had an average $\delta^{18}O$ value of −19·3‰ and $\delta^{13}C$ value of −1·8‰.

DISCUSSION

Ground and surface waters

A survey of key waters in the study area provided estimates for the evaporative losses of playa waters and an understanding of the hydrogeochemistry as it relates to carbonate precipitation. The main wetland in the southeastern playa does not have any surface water tributaries or outlets and, therefore, the water balance consists of input from precipitation and groundwater, and output via evaporation. The intersection between the local evaporation line (LEL) and meteoric water line (Fig. 3A) is a good estimate of the weighted mean isotopic composition of annual precipitation of a catchment, which is reflected in the H and O isotopic compositions of the groundwater (Gibson *et al.*, 1993). This intersection occurs approximately at a δ^2H value of −173‰ and a $\delta^{18}O$ value of −22‰ (Fig. 3A). The spring water, well water and surface water from many of the small isolated ponds have δ^2H and $\delta^{18}O$ values that are close to the isotopic composition of mean groundwater. This similarity may signify the transient nature of the water present in these small ponds, i.e. there is frequent replenishment of groundwater, possibly due to flow
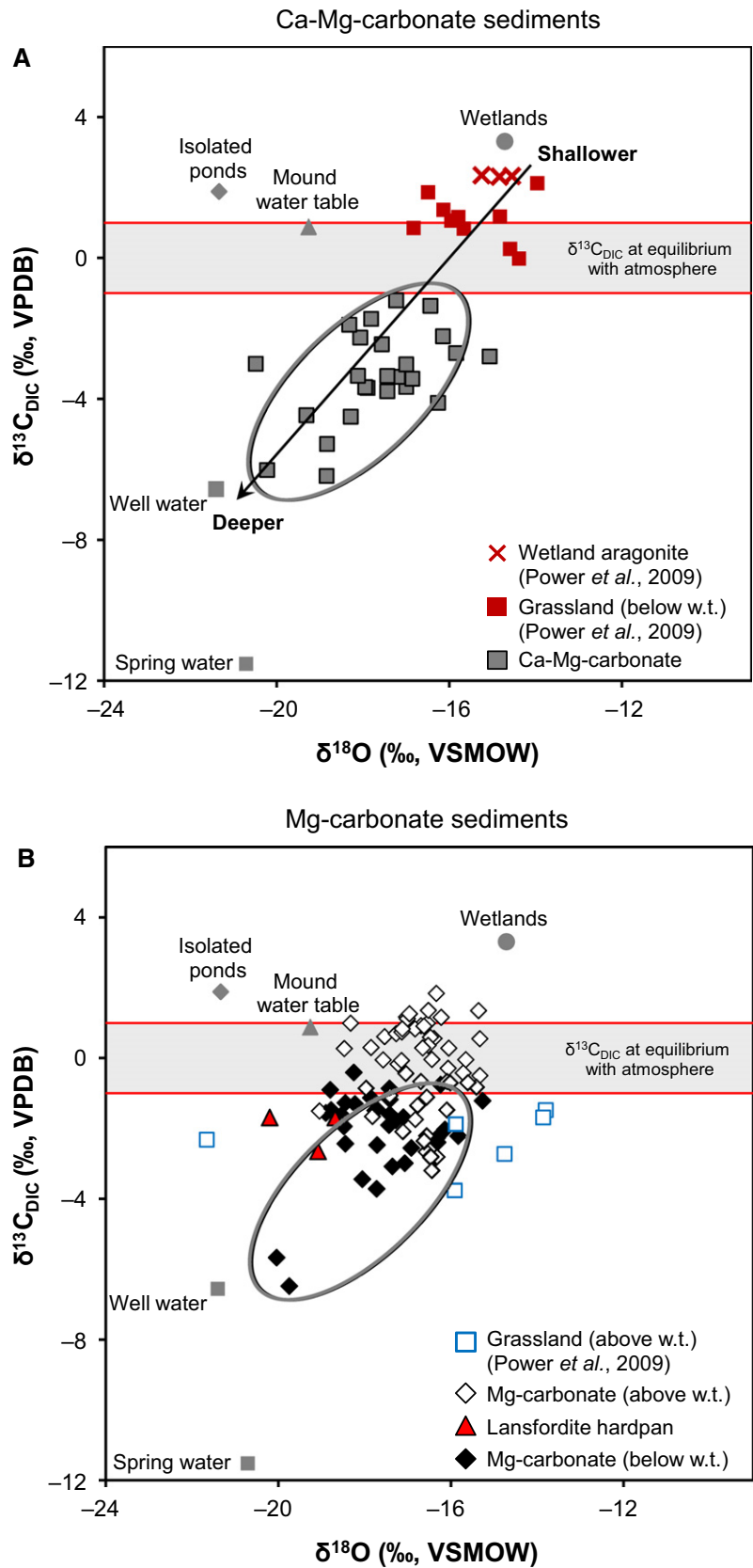
Fig. 11. (A) Plot of $\delta^{13}C_{DIC}$ and $\delta^{18}O$ values of waters for precipitating the Ca–Mg-carbonate sediments based on equilibrium fractionation. (B) Plot of $\delta^{13}C_{DIC}$ and $\delta^{18}O$ values of waters for precipitating Mg-carbonate sediments based on equilibrium fractionation. The average carbon and oxygen isotopic compositions of the waters in Fig. 3B are plotted for comparison. Isotopic data of the wetland aragonite and grassland sediments (above and below the water table) are from Power *et al.* (2009).

towards the main wetland. The slightly acidic groundwater (pH 6 to 7; Power *et al.*, 2009) in the grassland may be mobilizing Ca, resulting in the greater Ca concentrations detected in these isolated ponds.

Evapoconcentration of ions is important for driving carbonate precipitation in the playas. The slope of a LEL reflects the influence of varying local conditions (for example, temperature, humidity, wind speed, fetch, etc.) that are naturally integrated over the evaporation dominated season. Relative displacement along the LEL for a given evaporation rate is characteristic of local conditions, as is the limiting enrichment, i.e. the maximum enrichment expected due to evaporation without a reduction in water volume (Gibson *et al.*, 1993). Calculated evaporative losses for water samples collected from the water table at sediment profile locations 4, 6 and 7 are between 10% and 20%. Evaporative losses calculated for water samples collected from the wetlands in the south-eastern playa are between 30% and 65%. Comparison of the Na and Cl concentrations in the groundwater and wetland water suggests an evapoconcentration of *ca* 300 to 500%. These values may reflect an accumulation of ions over several years to reach a steady state, whereas isotopic data reflect yearly evaporative losses. The data demonstrate the variability in evapoconcentration of waters in these closed basins.

Ground and surface waters from the field site are essentially Mg–HCO$_3$ waters with relatively minor concentrations of other elements (for example, Ca). Most waters are supersaturated with respect to aragonite, calcite, dolomite, huntite and magnesite as calculated using PHREEQC (Parkhurst & Appelo, 1999; Table 2). The water table within the amalgamated mound is undersaturated with respect to aragonite and calcite. Waters from the water table at the location of sediment profile 4 and the main wetland that is adjacent to the mound are also supersaturated with respect to lansfordite and hydromagnesite. All waters are undersaturated with respect to nesquehonite; however, the north and south lobes of the main wetland are closest to nesquehonite saturation with saturation indices (SI) of −0·49 and −0·54, respectively. Solubility data are not available for dypingite. Although Mg-silicate clays, such as sepiolite [Mg$_4$Si$_6$O$_{15}$(OH)$_2$ · 6H$_2$O], are supersaturated in wetland water, there is no accumulation that is detectable by XRD. Biological uptake is probably the main sink for dissolved silicon (Power *et al.*, 2007).

The stable carbon and oxygen isotopic compositions of the Atlin waters show enrichment in both ^{13}C$_{DIC}$ and ^{18}O moving towards the main wetland (Fig. 3B). Firstly, there is enrichment in ^{13}C of the well water relative to the spring water. The δ^{13}C and δ^{18}O values for the carbonate minerals in the magnesite, talc and quartz zones of the listwanite (carbonated serpentinite) in the Atlin region range from *ca* −7 to −1‰ VPDB and from *ca* 6 to 16‰ VSMOW, respectively (Hansen, 2005). A simple mixing model that takes into account the δ^{13}C values of the spring water and bedrock magnesite, and the increase in DIC concentration from the spring water to the well water results in δ^{13}C$_{DIC}$ values between −5‰ and −6‰, which is reasonably close to the average δ^{13}C$_{DIC}$ of −6·6‰ for the well water. This mixing model assumes complete dissolution of magnesite rather than equilibrium isotopic exchange. Thus, as groundwater moves towards the playas, there is probably dissolution of bedrock carbonate contributing to DIC. Relative to the well water, there is further enrichment of ^{13}C in the water samples collected from the playa, which is probably attributable to CO$_2$ degassing and exchange with the atmosphere (Zedef *et al.*, 2000). Dissolved inorganic carbon (DIC) in equilibrium with atmospheric CO$_2$ has a δ^{13}C value of *ca* 0 ± 1‰ assuming a δ^{13}C value of −8 ± 1‰ for bulk atmospheric CO$_2$ (Keeling *et al.*, 2005) and an equilibrium fractionation factor between CO$_{2(g)}$ and HCO$_{3(aq)}^-$, the dominant aqueous carbonate species in the documented pH range, of +7·9‰ at 25°C (Mook *et al.*, 1974). Waters from the playa have δ^{13}C$_{DIC}$ values ranging from 0 to 5‰, indicating that these waters are either at isotopic equilibrium with atmospheric CO$_2$ or relatively enriched in ^{13}C. High primary bioproductivity can also enrich DIC in ^{13}C as there is preferential uptake of ^{12}C during photosynthesis by algae and cyanobacteria (Melezhik *et al.*, 2001). The microbial mats, observed within the wetlands and isolated ponds, may explain the carbon isotope compositions of these waters having δ^{13}C values above those expected for isotopic equilibrium with the atmosphere. The second prominent trend is the progressive enrichment in ^{18}O (−22 to −13‰) relative to the groundwater that can be attributed to evaporation as previously discussed. The chemical and isotopic compositions of the playa waters evolve due to dissolution of the surrounding bedrock, CO$_2$ degassing and exchange with the atmosphere, photosynthetic

uptake of ^{12}C and progressive evapoconcentration in these closed basins.

Playa genesis model

The detailed analyses of the sediments in the Atlin playas allow for a better understanding of the modes of sediment deposition and the environmental conditions at the time of deposition. The surface of the south-eastern playa is at different stages of development that are typified by four distinct areas: wetlands, grasslands, localized mounds and amalgamated mounds (see aerial photograph in Fig. 2A). A schematic model (Fig. 12) is referenced in the following discussion to illustrate playa genesis through time. The playa genesis model is divided into three stages: (i) deposition occurring in a subaqueous depositional environment, for example lakes and wetlands; (ii) deposition coincident with the 'emergence' of sediments from the water surface, for example the transition from subaqueous to subaerial deposition; and (iii) mound growth and amalgamation.

Deposition in a subaqueous environment

The playas lie in topographic lows that were probably carved out by glaciers during the last glaciation (Fig. 12A). The Cordilleran ice sheet covered nearly all of British Columbia, southern Yukon, southern Alaska and the north-western conterminous United States. The ice sheet reached a maximum size at *ca* 16·5 ka and had disappeared by 11 ka (Menounos *et al.*, 2009, and references therein). In the Atlin area, surficial glacial deposits are common (Levson, 1991). For instance, glacial till is found underneath a thin veneer of soil on the ridge that separates the south-western and south-eastern playas and it is presumed that glacial deposits underlie the playas. During deglaciation, glacier meltwater probably formed lakes in the topographic lows that are now occupied by the playas. Although uncommon, glaciolacustrine deposits are present at the surface in the Atlin area and are described by Levson (1991) as cohesive, impermeable silts and clays that are horizontally laminated to massive. The siliciclastic mud found at the base of some of the sediment profiles is consistent with this description, and therefore is almost certainly a glaciolacustrine deposit (Fig. 12B). Following deglaciation, the supply of glacial meltwater and detrital sediments would have ceased.

Alkaline groundwater would have become the dominant water supply discharging into the topographic lows. This marked a major change in the hydrogeochemistry of these water bodies; transitioning from fresh surface water to Mg–HCO$_3$ groundwater that is produced from the weathering of ultramafic rock in the region. The present-day wetlands in the south-eastern playa are remnants of a larger water body, which is consistent with the 'pond hypothesis' originally proposed by Young (1916) to explain playa genesis near Atlin. The main wetland water is supersaturated with respect to aragonite, calcite, dolomite, huntite, hydromagnesite, lansfordite and magnesite (Table 2); however, precipitation of many of these minerals is likely to be kinetically inhibited. Waters with high Mg/Ca ratios, such as the wetland, favour the precipitation of aragonite due to a decrease in calcite growth rates (De Choudens-Sánchez & González, 2009). At low temperatures, magnesite and dolomite are known to be kinetically inhibited. Hydromagnesite may also be kinetically inhibited; commonly requiring temperatures >40°C to precipitate in laboratory studies (Königsberger *et al.*, 1999; Hänchen *et al.*, 2008). Lansfordite typically forms at temperatures below 10°C (Königsberger *et al.*, 1999). As such, carbonate precipitation in these environments is controlled more so by kinetics than solubility.

Within the modern wetland, there are abiotic and biotic reaction pathways for precipitating Ca-carbonate and Mg-carbonate minerals (Fig. 12C; Power *et al.*, 2007). Evapoconcentration of wetland water forms nesquehonite films on the water surface and dypingite precipitates within benthic microbial mats (Fig. 4A and B; Power *et al.*, 2007, 2009). However, variability of pH in the water column and pore water of sediments may favour the preservation of Ca-carbonate minerals in the sediments. Anoxic sediments below the benthic microbial mats are composed almost entirely of aragonite in the main wetland (Power *et al.*, 2009). The decomposition of organic matter in these sediments generates acidity that may cause metastable carbonate minerals to dissolve upon burial (e.g. Walter *et al.*, 1993; Deocampo & Ashley, 1999). Pore water in the anoxic sediments, measured at pH 7·8, is further undersaturated with respect to nesquehonite in comparison to the bulk wetland water (pH ≈ 8·6); however, aragonite remains supersaturated (Parkhurst & Appelo, 1999). Ultimately, carbonate accumulation within wetlands causes progressive infilling of features over relatively short periods (for example, Fig. 4B). This implies that there is a fairly rapid sedimentation
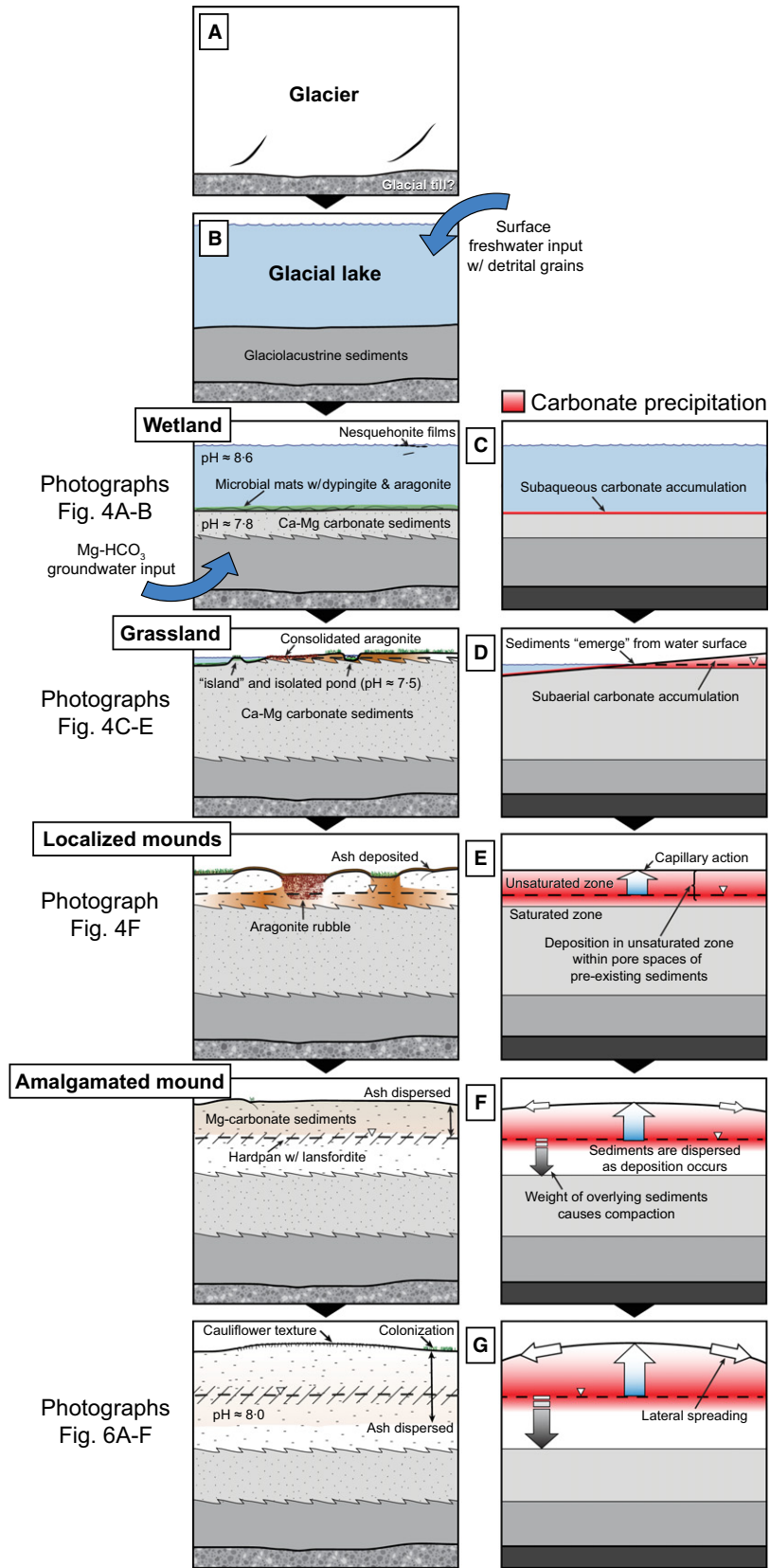
Fig. 12. Conceptual schematics illustrating features (left column) and modes of deposition (right column) during various stages of playa genesis. (A) Topographic lows are carved out by glaciers. (B) During deglaciation, meltwater forms glacial lakes in which glaciolacustrine sediments are deposited. (C) Water body changes from surface water to alkaline groundwater fed; deposition shifts from siliciclastic to primarily chemical carbonate precipitation. (D) Topographic lows progressively infill leading to the eventual 'emergence' of sediments from the water surface and, in some cases, isolating portions of wetland. Consolidated aragonite containing pisolites may form in some locations along the periphery of water bodies. (E) Capillary action draws water upwards and evaporation drives Mg-carbonate precipitation, leading to the development of localized hydromagnesite mounds (metre-scale). (F) Localized mounds amalgamate into larger mounds and underlying sediments become compacted. A lansfordite hardpan develops near the water table. An amalgamated mound continues to grow upwards and may spread laterally. Also presented in (E) is the deposition of a volcanic ash layer that becomes progressively more dispersed, shown in (F) and (G), as the mounds grow.

rate in the main wetland, possibly in the order of centimetres per year of loose sediment. Intuitively, water bodies in the playas gradually fill over time.

Deposition coincident with emergence of sediments from water surface
Progressive infilling of the wetlands would eventually lead to sediments 'emerging' from the water surface, marking a shift from a subaqueous to a subaerial depositional environment (Fig. 12D). Emergence of sediments from the water surface leads to the development of an unsaturated zone, albeit that this is initially very thin. Because the material is fine grained, capillary action and evaporation draw Mg–HCO$_3$ water towards the surface of the sediments. This represents a distinct change in the geochemical environment and thus significantly influences carbonate precipitation. Hydrated Mg-carbonate minerals are known to form as a result of evaporative concentration of ions in unsaturated zones containing Mg-rich waters (e.g. Wilson *et al.*, 2009a, 2011; Bea *et al.*, 2012). Previous analysis of the near-surface sediments along the wetland periphery determined that these are composed of dypingite and nesquehonite (Power *et al.*, 2009). Sediments below the surface are granular and stained orange by iron oxyhydroxides, indicating oxic conditions. In some locations near the wetland periphery, there is consolidated aragonite rubble (Fig. 4C). Pisolites with inverse-graded bedding indicate formation in an unsaturated (vadose) zone (Esteban, 1976; Jin & Bergman, 1999). Pisolites are composed of pisoids, which are coated grains composed of calcium carbonate that are similar to ooids, but >2 mm in diameter. Consolidated aragonite rubble is found in numerous other locations in the southeastern playa and in the northern playa, indicating that similar conditions existed in the past.

Grasslands are interpreted to represent an intermediate environment between the wetlands and mounds. Nutrient-rich sediments that become exposed at the ground surface are colonized by grasses. Tufts of grasses reinforced by carbonate sediments form 'islands' within the wetlands and appear to eventually merge and isolate sections of the larger wetland to form small, isolated ponds (Fig. 4D and E). Previous sampling of the grassland sediments at depth showed that there is a mineralogical change between Mg-carbonate sediments (hydromagnesite) near the surface and sediments consisting of aragonite and ankerite slightly below (*ca* 10 cm) the water table (Power *et al.*, 2009). X-ray diffraction patterns of these sediments had broad peaks, suggesting either or both poor crystallinity and variable composition. This transition to sediments with Ca-bearing carbonate minerals with poor crystallinity is similar to the changes in mineralogical composition that are observed at depth in the sediment profiles sampled in this study; however, this boundary was noted further below the water table (average depth ≈ 2 m from surface). There is strong evidence to suggest that these two mineralogical shifts are related to one another. The Ca–Mg-carbonate sediments and underlying glaciolacustrine sediments contain diatom frustules, remnants of photosynthetic microbes, implying that these sediments were deposited in a subaqueous environment (i.e. open water) and, conversely, that the Mg-carbonate sediments that do not contain diatom frustules were deposited post-emergence from the water surface. Furthermore, the difference in colouration between the white Mg-carbonate sediments and the dark Ca–Mg-carbonate sediments is a visible indication of the shift in depositional environments. In a subaqueous environment, there is an accumulation of organic matter and iron sulphides in the

sediments giving them a dark colouration. The white Mg-carbonate sediments lack organic matter and sulphide minerals, which can only occur in a subaerial environment where organic matter does not accumulate and the presence of oxygen inhibits the formation of sulphide minerals.

Field observations indicate that deposition of carbonate near the surface may be outcompeting growth of grasses. The availability of essential nutrients such as nitrate and phosphate is limiting in calcareous soils (Hancock *et al.*, 2011; Hosseinpur *et al.*, 2012). Continued carbonate accumulation further dilutes nutrients making it difficult for vegetation to survive. The remnant vegetation, discovered near the top of the Ca–Mg-carbonate sediments in profiles 6 and 7, has $\delta^{13}C$ values (average = $-22 \cdot 5‰$) in the range of C_3 vegetation (Cerling *et al.*, 1997) and are comparable to the $\delta^{13}C$ value of modern grass ($-27 \cdot 3‰$) in the south-eastern playa (Power *et al.*, 2009). Remnant vegetation within the amalgamated mound is indicative of a palaeosol that has become buried by Mg-carbonate sediments. As a result, the hydromagnesite–magnesite mounds probably formed atop the grassland sediments in a subaerial environment, as evidenced by the lack of organic matter and iron sulphide minerals, absence of diatom frustules, and the presence of buried of grasses found near the Ca–Mg-carbonate boundary.

Mound growth and amalgamation
The localized and amalgamated mounds are dominant features of the playas (Fig. 12E). It is not known what causes the placement of a mound in a particular location. The presence of greater amounts of carbonate, i.e. the mound itself, suggests greater evaporation and/or more favourable geochemical conditions for carbonate precipitation. This may relate to sediment properties in relation to ground water discharge and evaporation, which may perpetuate carbonate deposition. For instance, tufa mounds are known to form at locations of active groundwater discharge (Keppel *et al.*, 2012).

Field observations suggest that there is both upward and lateral growth of these mounds as carbonate sediments accumulate. Intuitively, the topographic relief of these mounds suggests upward growth. The unusual placement of serpentinite stones (Fig. 6F) on top of Mg-carbonate sediments, as first recognized by Young (1916), may be due to the gradual carbonate precipitation underneath these stones causing them to be lifted so as to 'float' on the surface. Smaller localized mounds (metre-scale) appear to be amalgamating into larger mounds that are tens of metres in width. In some of the amalgamated mounds, grasses delineate what were probably once outer boundaries of localized mounds. This is most easily observed in aerial photographs (see right-hand side of Fig. 2A). As the mounds grow upwards, the weight and ductile nature of the sediments seem to cause them to flow laterally, albeit very slowly (Fig. 12F). There is qualitative evidence of mass movement, such as slumping, evidenced by the traverse cracks seen on the amalgamated mound (Fig. 6D).

The lansfordite hardpan provides insight as to the internal growth of the mounds. Lansfordite was first documented in Atlin by Poitevin (1924) who found it at a depth of *ca* 1 m in the south-western playa. Water at the water table is supersaturated with respect to lansfordite and its precipitation cements pre-existing sediments. This hardpan is laterally extensive and analogous to calcrete (or caliche) hardpans that form by groundwater evaporation in arid and semi-arid regions (Kholodov, 2007; Eren & Hatipoglu-Bagci, 2010). Lansfordite is the most hydrated Mg-carbonate mineral found in the playas, and its abundance near the water table suggests that it may be a primary precipitate. It should be noted that hydromagnesite precipitation is thought to be possibly kinetically inhibited at temperatures found below the ground surface (Königsberger *et al.*, 1999; Hänchen *et al.*, 2008). Presumably, capillary action draws Mg–HCO$_3$ water from the water table towards the ground surface, probably allowing for carbonate precipitation over a wide range of depths. The occurrence of polygonal versus cauliflower desiccation cracking (Fig. 6A) relates to the moisture content of the sediment, which in turn relates to the distance from the water table to the surface with cauliflower desiccation cracking typically occurring at higher elevations. In almost all of the sediment profiles, the abundance of magnesite decreased near the water table. This suggests either that magnesite does not form near the water table or that precipitation of hydrated Mg-carbonate minerals dilutes magnesite abundance.

Ecological succession is perhaps the final stage in modern playa genesis. The relative rates between carbonate precipitation and growth of vegetation varies over the development of the playas. When organic-rich and nutrient-rich sediments emerge from the water surface, growth of

vegetation initially exceeds carbonate deposition, yet continued carbonate deposition buries vegetation. In some of the amalgamated mounds, grasses are now beginning to colonize the surface indicating that the very top surface has become stagnant for a long enough period for nutrient levels to increase sufficiently to support vegetation. Growth and decay of cyanobacteria may increase nutrient levels over time and eventually allow for colonization by grasses. Grasses are seen colonizing polygonal cracks, possibly mimicking the growth patterns of cyanobacteria. Grasses are more extensive on the northern playa surface indicating that this playa is further developed.

Sediment compaction

Magnesium-carbonate sediments are present both above and below the water table in the amalgamated mound (Fig. 12G). A shift from Mg-carbonate sediments to the Ca–Mg-carbonate sediments is seen at an average depth of 1 m below the water table, whereas a similar shift in the grassland sediments coincided with the water table (Power *et al.*, 2009). A possible explanation for this discrepancy is sediment compaction caused by the weight of overlying sediments. This sort of autocompaction occurs by syn-depositional and post-depositional diagenetic processes that result in the mechanical reduction in bulk volume or porosity of sediments (Brain *et al.*, 2011). Mechanical compaction of muddy carbonate sediments can result in significant thickness reduction early in the burial history and at shallow depths (Goldhammer, 1997). The ratio of the thickness of the Mg-carbonate sediments from the water table to the transition to Ca–Mg-carbonate sediments and the thickness of the Ca–Mg-carbonate sediments is *ca* 1 : 1 (see Fig. 9, profile 4). Because water is incompressible, the assumption is that water is expelled during the compaction of these water saturated sediments. If the position of the present-day water table is similar to a past water surface, then the thickness of the Mg-carbonate sediments below the water table indicates the amount of compaction that has occurred. The presence of aragonite in near-surface sediments close to the wetland (Fig. 5) suggests that the thickness of the Mg-carbonate unit becomes progressively thinner towards the outer edges (Fig. 9), which is consistent with compaction being proportional to the overlying thickness (i.e. weight) of the Mg-carbonate sediments.

An alternative hypothesis for the placement of the Mg-carbonate sediments below the water table is that of a rising water table throughout the development of the playa. However, at the base of profile 2, there is a mixture of Ca–Mg-carbonate and glaciolacustrine sediments that suggest that a water body would have extended at least to this point. These sediments correspond to the depth of the present-day water table, indicating that the modern water table may be representative of the past water surface of the alkaline water body. Furthermore, glaciolacustrine sediments extend to the very edge of the playa, signifying that a glacial lake was probably larger than the alkaline water body.

Sediment dispersal and carbonate accumulation rate

Carbonate precipitation within the pore spaces of pre-existing sediments results in dispersal of those sediments over time. This process is exemplified by the dispersal of ash particles within the amalgamated mound. Although volcanic ash is typically deposited as a discrete layer, ash particles were observed over a wide range of depths from the ground surface to 1·5 m depth in the Mg-carbonate sediments. This dispersal is symptomatic of precipitation occurring over a wide range of depths, rather than as discrete layers.

The late Holocene White River Ash is well-documented in Yukon and northern British Columbia (e.g. Richter *et al.*, 1995; Lakeman *et al.*, 2008). The extent of the White River Ash from Lerbekmo (2008) is shown on the map in Fig. 1A, yet other studies have documented this ash at greater distances than the Atlin site (e.g. Lakeman *et al.*, 2008; Addison *et al.*, 2010; see Fig. 1A). Atlin is *ca* 500 km from Mount Churchill and the fine particle size of the ash particles (<63 μm) is consistent with a distal source. The ash particles have a similar chemical composition to the White River Ash sample analysed in this study as well as analyses of the White River Ash by Downes (1985), Béget *et al.* (1992), Richter *et al.* (1995) and Lakeman *et al.* (2008). This implies that there has been *ca* 1·5 m of Mg-carbonate deposition since the deposition of the White River Ash dated at *ca* 1150 cal yr BP (Clague *et al.*, 1995). This equates to an average carbonate accumulation rate of *ca* 1·3 mm yr^{-1}.

The average depths and ages of the remnant vegetation for profiles 6 (296 cm/8045 yr) and 7

(243 cm/6527 yr) equate to a carbonate accumulation rate of 0.4 ± 0.01 mm yr^{-1}. The two estimated rates for carbonate accumulation in the amalgamated mound are similar to that of Chappice Lake (playa with hydromagnesite + detrital clays) in Alberta, Canada, of *ca* 1.2 mm yr^{-1} (Vance *et al.*, 1992), but considerably lower than for a hypersaline lake such as Freefight Lake, Saskatchewan, Canada, that has a sedimentation rate of 50 to 400 mm yr^{-1} (Last, 1993). The estimated accumulation rate based on the radiocarbon analyses of the remnant vegetation is an overall rate for the deposition of the Mg-carbonate sediments, whereas the estimated rate based on the volcanic ash particles accounts only for the top 1.5 m of Mg-carbonate sediments. The difference in estimated sedimentation rates may indicate that sediment accumulation has increased since the deposition of the White River Ash or may reflect variable compaction, i.e. less compaction at the top of the sediment column. Porosity loss is often described as an exponential function of stress (e.g. Croizé *et al.*, 2010), i.e. compaction of sediments would not be linear with the load applied.

Occurrence of magnesite and dolomite

Magnesite and dolomite precipitation are both kinetically inhibited at near-surface temperatures due to the strong hydration of Mg^{2+} ions in solution (Land, 1998; Königsberger *et al.*, 1999). Yet, the presence of magnesite and dolomite within the near-surface sediments of the playas in the context of the depositional model is clear evidence of low-temperature formation. The study of magnesite precipitation at low temperatures (for example, <60°C) has proven difficult given the kinetic inhibitions (Christ & Hostetler, 1970; Königsberger *et al.*, 1999; Hänchen *et al.*, 2008; Saldi *et al.*, 2012). The transformation of hydromagnesite to magnesite, the most stable Mg-carbonate phase, is thought to require in the order of tens to hundreds of years at near-surface conditions (Zhang *et al.*, 2000). This seems reasonable for magnesite formation within the playa sediments, which have temperatures that are less than *ca* 15°C during the summer. Although the playas are considered 'modern', carbonate deposition has probably been occurring since shortly after the end of the last glaciation (*ca* 11 ka). As such, it is difficult to constrain the rates of magnesite and dolomite formation, which may have occurred post-deposition through the diagenesis of minerals such as aragonite (found in wetland sediments) and hydrated Mg-carbonate minerals, lansfordite (hardpan), dypingite and nesquehonite (wetland periphery). Conversely, magnesite appears as a separate phase when viewed using SEM and, therefore, may be precipitating directly from solution.

Insights from isotopic markers

Interpretation of the isotopic compositions of the carbonate sediments must be carried out in the context of the depositional model. During initial precipitation, the isotopic composition of carbonate minerals is generally dependent upon the isotopic composition and temperature of the water from which they precipitate, and the mineralogical composition of the resulting precipitate (for example, hydromagnesite versus aragonite). However, continued carbonate precipitation within the pore spaces of pre-existing sediments may alter the bulk isotopic composition of the sediments, causing an 'overprinting' or 're-setting' of the original isotopic signal if the geochemical conditions have changed over time. Beginning with the wetland aragonite that is near isotopic equilibrium with wetland water, there is relative depletion in ^{18}O and ^{13}C of the grassland sediments below the water table (mainly aragonite and ankerite) and even further depletion in the Ca–Mg-carbonate sediments (Fig. 11A). This trend could be explained by post-depositional diagenesis, such as precipitation of ankerite, magnesite and/or dolomite from groundwater that is relatively depleted in ^{18}O and ^{13}C compared to surface waters. In this case, aragonite is a primary precipitate that has since undergone transformation to or replacement by other minerals (for example, ankerite and dolomite). The abundance of amorphous carbonate in the Ca–Mg-carbonate sediments is further indication of the precipitation of poorly crystalline phases and/or of alteration of pre-existing minerals. Similarly, the isotopic compositions of Mg-carbonate sediments may also reflect a range of isotopic compositions from groundwater to near-surface pore water in the unsaturated zone (Fig. 11B). For instance, Mg-carbonate sediments collected below the water table precipitated from waters that generally had $\delta^{13}C_{DIC}$ values below isotopic equilibrium with atmospheric CO_2; the opposite is true of samples collected above the water table (Fig. 11B). Waters with a range of isotopic compositions must be considered when interpreting the isotope data of the

carbonate sediments in the sediment profiles (Fig. 10).

At the boundary between the Mg-carbonate and Ca–Mg-carbonate sediments, there is a noticeable enrichment in ^{18}O and ^{13}C (Fig. 10) in the Mg-carbonate sediments relative to the underlying Ca–Mg-carbonate sediments. The difference in equilibrium fractionation of ^{18}O between hydromagnesite-water and aragonite-water is *ca* +2·5‰ (Tarutani *et al.*, 1969; O'Neil & Barnes, 1971), whereas the difference in equilibrium fractionation of ^{13}C between hydromagnesite-CO_2 and aragonite-CO_2 is +1 (Rubinson & Clayton, 1969; Mook *et al.*, 1974). Thus, the changes in the overall mineralogical composition between the Mg-carbonate sediments and underlying Ca–Mg-carbonate sediments are one possible explanation of the observed differences in $\delta^{18}O$ and $\delta^{13}C$ values at the boundary between these two units (Fig. 10A and B). However, a more likely explanation for the enrichment of ^{18}O and ^{13}C in the Mg-carbonate sediments is evaporation and CO_2 degassing, respectively, that would accompany a shift to subaerial deposition as proposed by the depositional model in this study.

The trends seen in the isotopic data for the sediments profiles (Fig. 10) most closely aligned with one another when data were plotted in relation to the water table as opposed to the ground surface. This implies that proximity to the water table has a significant influence on the isotopic composition of the carbonate sediments, particularly with the $\delta^{13}C$ values. Examination of the isotopic compositions of the grassland sediments reported by Power *et al.* (2009) (Fig. 10C and D) is helpful in the interpretation of the isotopic data of the amalgamated mound (Fig. 10A and B). The grassland sediments near the surface provide a snapshot of the sediment isotopic values at the initial stages of subaerial Mg-carbonate deposition. It should be noted that the growth of grasses does not affect stable oxygen isotopes because there is no ^{18}O fractionation during the uptake of water by plants (Barbour, 2007). The average $\delta^{18}O$ and $\delta^{13}C$ values show a +5‰ enrichment in ^{18}O and a relatively insignificant effect on ^{13}C for the Mg-carbonate sediments relative to the underlying Ca–Mg-carbonate sediments in the grassland (Fig. 10C and D). These data suggest that post-emergence, subaerial Mg-carbonate precipitation results in significant enrichment in ^{18}O due to evaporation near the surface, but little or no enrichment in ^{13}C. In the amalgamated mound, similar $\delta^{18}O$ values of Mg-carbonate sediments (up to 19·7‰) are observed near the surface, suggesting that proximity to the surface influences ^{18}O compositions, owing to CO_2 degassing and exchange with the atmosphere (Spötl *et al.*, 2002). The Mg-carbonate sediments at the grassland surface have similar $\delta^{13}C$ values to Mg-carbonate sediments near the water table in the amalgamated mound, which suggests that proximity to the water table has a strong influence on the ^{13}C composition of Mg-carbonate minerals. The lansfordite hardpan may be representative of more recent precipitation near the water table. Progressive enrichment of ^{13}C in the Mg-carbonate sediments accompanies the growth of the mound as the thickness of the unsaturated zone becomes greater, thereby allowing greater CO_2 degassing and exchange with the atmosphere. Noteworthy are the $\delta^{13}C$ values of profile 2 that were lowest *ca* 50 cm above the modern water table, whereas the lowest $\delta^{13}C$ values of the other profiles corresponded to near the water table (Fig. 10B). This discrepancy may indicate that the water table was higher in the past, allowing for Mg-carbonate deposition in the location of profile 2.

Comparison to similar carbonate systems

The depositional model presented in this study is consistent with observations from similar carbonate systems. Carbonate sedimentary sequences have been used to reconstruct changes in water composition through time (Last & Last, 2012). For example, a shift from calcite to aragonite precipitation in sediment cores from Great Salt Lake, Utah, has been interpreted as being caused by a shift to higher Mg/Ca ratios in palaeolake waters (Spencer *et al.*, 1984). Renaut (1993) studied hydromagnesite–magnesite playas of the Cariboo Plateau in British Columbia, Canada. In some instances, a similar sedimentary sequence to that in Atlin was noted: hydromagnesite and magnesite muds overlying sediments containing non-stoichiometric dolomite, aragonite, Mg-calcite and calcite at depths greater than *ca* 30 cm. These carbonate sediments had a sharp contact above several decimetres of dense clay, which overlay glaciofluvial sands and gravels. A possible explanation for the mineral stratigraphy in the Cariboo Plateau playas may be increasing Mg/Ca ratios of water through time, shifting the dominance from Ca-bearing to Mg-bearing carbonate precipitation. However, in Atlin, a better explanation is a change in the depositional environment rather than a change

in water chemistry. Although the present-day water composition of the main wetland has a Mg/Ca ratio of *ca* 150, kinetic effects inhibit the precipitation of many carbonate minerals and there is preferential preservation of calcium carbonate minerals. Consequently, aragonite, rather than Mg-carbonate minerals, is the major constituent of sediments below the benthic mats within the wetland, whereas the precipitation of hydromagnesite–magnesite sediments occurs in a subaerial environment.

Subaerial precipitation of Mg-carbonate minerals has also been noted in similar environments. A 7000-year record of lake-level changes is captured in the sedimentary fill of Chappice Lake, a shallow, saline playa lake in south-eastern Alberta, Canada (Vance *et al.*, 1992). There is a suite of carbonate minerals from an 8 m thick sequence comprised of magnesite, hydromagnesite, aragonite and dolomite, which are interbedded with siliciclastic sands and silts. Low-water intervals indicating periods of drought were recorded by the presence of carbonate units, with hydromagnesite being particularly abundant (Vance *et al.*, 1992). Periods of complete drying of the lake are signified by layers of fine sand and silt with mudcracks. Although not suggested by Vance *et al.* (1992), units of predominately hydromagnesite may have formed through capillary rise and evaporation of Mg-rich waters in a subaerial environment. Other researchers have also documented subaerial precipitation of Mg-carbonate minerals. For instance, Détriché *et al.* (2013) studied the Late Holocene Lake Afourgagh sediment record showing that the littoral zone is comprised predominately of magnesite. It was suggested that magnesite was formed by diagenesis of a precursor that precipitated from capillary evaporation of shallow ground waters. Yet another example is the hardgrounds containing hydromagnesite and magnesite that have been documented from East Basin Lake in southern Australia (Last, 1992).

Hydrated Mg-carbonate minerals are metastable and may transform to magnesite over geological timescales (Hänchen *et al.*, 2008; Hopkinson *et al.*, 2008). For example, the Upper Permian Gröden Formation of the Northern Calcareous Alps in Austria is composed of alluvial fan and playa lake deposits with magnesite nodules and layers being found in mudstones (Spotl & Burns, 1994). Shrinkage features are associated with magnesite, suggesting that it formed from the transformation of a hydrated Mg-carbonate. Like Atlin, stable isotopic data suggest mineralization
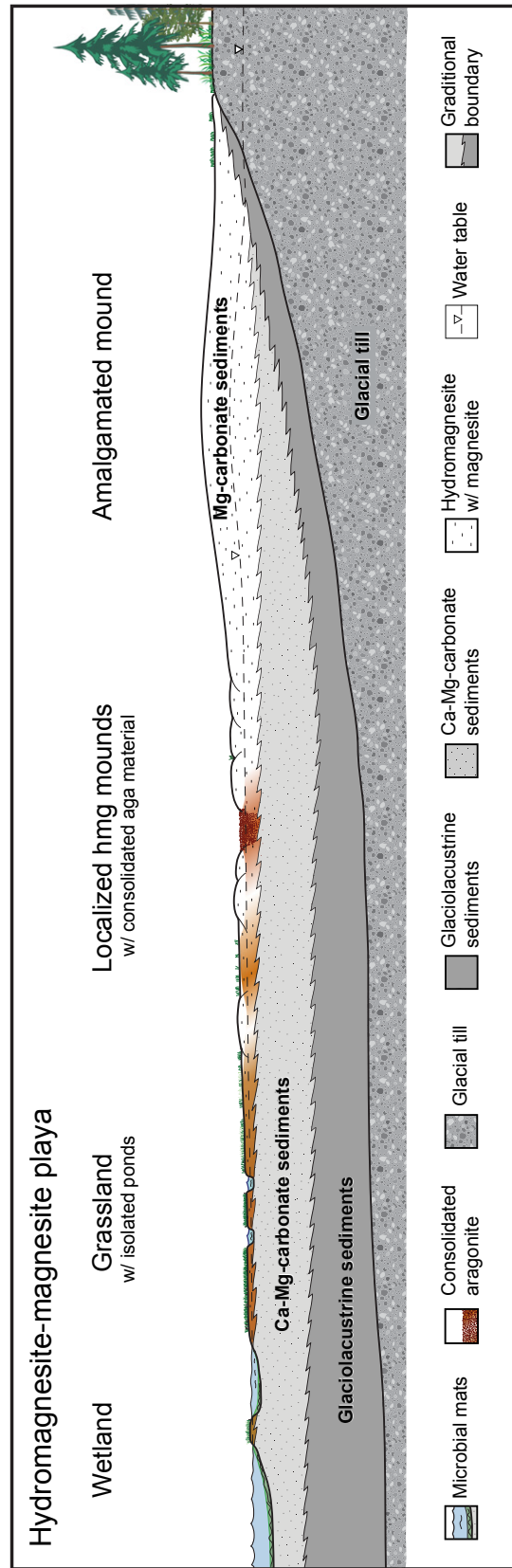

Fig. 13. A conceptual diagram illustrating the four surface environments and sedimentary units of the hydromagnesite–magnesite playas near Atlin.

within an inland playa lake system fed by low-sulphate, high Mg/Ca ratio waters (Spotl & Burns, 1994). At Atlin, high abundances of magnesite and dolomite have formed over a relatively short time period (<11 ka) and may become dominant minerals in the sediments over geological time.

CONCLUSIONS

The modern surface environments (wetlands, grasslands, localized mounds and amalgamated mounds) in the south-eastern playa represent four stages in playa genesis and were informative in constructing the depositional model for the hydromagnesite–magnesite playas (Figs 12 and 13). Subsurface sampling revealed three sedimentary units: siliciclastic mud, Ca–Mg-carbonate sediments and Mg-carbonate sediments. Changes in source water and depositional environment significantly impact the mineralogy of the sediments. A shift from siliciclastic deposition to primarily chemical carbonate precipitation occurred as the supply of fresh surface water ceased and was replaced by alkaline Mg–HCO_3 groundwater generated from the weathering of ultramafic bedrock.

Precipitation kinetics play a significant role in sediment deposition in open water bodies, such as in the modern wetlands. Preferential preservation of aragonite followed by burial and diagenesis may explain the variety of Ca-bearing carbonate phases observed in the sediment profiles at depth. Remnant vegetation near the top of the Ca–Mg-carbonate sediments clearly indicates that there was a transition from a subaqueous to a subaerial environment, which occurred once sediments infilled a water body and emerged from the water surface, thereby permitting colonization by grasses. This restricts the accumulation of hydrated Mg-carbonate minerals, primarily hydromagnesite, to a subaerial environment. Magnesite is the only mineral that occurs in both the Mg-carbonate sediments and the underlying Ca–Mg-carbonate sediments. The dispersal of volcanic ash particles over 1·5 m of Mg-carbonate sediments demonstrates the dynamic nature of sediment deposition in the mounds.

Although carbonate precipitation within the pore spaces of pre-existing sediments may complicate the interpretation of isotopic data, proximity to the water table is a strong influence on the stable carbon isotope values of the Mg-carbonate sediments. Radiocarbon dating of remnant vegetation indicates that there has been up to *ca* 8000 years of continuous Mg-carbonate deposition at a rate of 0·4 mm yr^{-1}. This long-term accumulation and preservation suggest a level of stability required for the storage of anthropogenic CO_2. Under near-surface conditions, the low solubilities of hydrated Mg-carbonate minerals at relatively alkaline pH limit dissolution (Königsberger *et al.*, 1999). In addition, mineralogical transformations to less-hydrated carbonate phases such as hydromagnesite and magnesite further enhance stability. In a carbon storage scenario, artificial sinks of anthropogenic CO_2 that mimic the conditions of the Atlin playas will be stable long enough to produce a greenhouse gas benefit.

ACKNOWLEDGEMENTS

REFERENCES

Addison, J.A., **Béget, J.E.**, **Ager, T.A.** and **Finney, B.P.** (2010) Marine tephrochronology of the Mt. Edgecumbe Volcanic Field, Southeast Alaska, USA. *Quatern. Res.*, **73**, 277–292.

Alcicek, H. (2009) Late Miocene nonmarine sedimentation and formation of magnesites in the Acigol Basin, southwestern Anatolia, Turkey. *Sed. Geol.*, **219**, 115–135.

Ash, C.H. and **Arksey, R.L.** (1990) The Atlin ultramafic allochthon: ophiolite basement within the Cache Creek Terrane; tectonic and metallogenic significance (104N/12). In: *Geological Fieldwork 1989*, Paper 1990-1, pp. 365–374. B.C. Department of Energy and Mines, Vancouver, BC.

Barbour, M.M. (2007) Stable oxygen isotope composition of plant tissue: a review. *Funct. Plant Biol.*, **34**, 83–94.

Barker, S.L.L., **Dipple, G.M.**, **Dong, F.** and **Baer, D.S.** (2011) Use of laser spectroscopy to measure the $^{13}C/^{12}C$ and $^{18}O/^{16}O$ compositions of carbonate minerals. *Anal. Chem.*, **83**, 2220–2226.

Bea, S.A., **Wilson, S.A.**, **Mayer, K.U.**, **Dipple, G.M.**, **Power, I.M.** and **Gamazo, P.** (2012) Reactive transport modeling of natural carbon sequestration in ultra-mafic mine tailings. *Vadose Zone J*, **11**.

Beavan, N., **Halcrow, S.**, **McFadgen, B.**, **Hamilton, D.**, **Buckley, B.**, **Sokha, T.**, **Shewan, L.**, **Sokha, O.**, **Fallon, S.**, **Miksic, J.**, **Armstrong, R.**, **O'Reilly, D.**, **Domett, K.** and **Chhem, K.R.** (2012) Radiocarbon dates from jar and coffin burials of the Cardamom Mountains reveal a unique mortuary ritual in Cambodia's Late- to Post-Angkor Period (15th-17th Centuries AD), *Radiocarbon*, **54**, 1–22.

Béget, J., **Mason, O.** and **Anderson, P.** (1992) Age, extent and climatic significance of the c. 3400 BP Aniakchak tephra, western Alaska, USA. *Holocene*, **2**, 51–56.

Brain, M.J., **Long, A.J.**, **Petley, D.N.**, **Horton, B.P.** and **Allison, R.J.** (2011) Compression behaviour of minerogenic low energy intertidal sediments. *Sed. Geol.*, **233**, 28–41.

Braithwaite, C.J.R. and **Zedef, V.** (1994) Living hydromagnesite stromatolites from Turkey. *Sed. Geol.*, **92**, 1–5.

Braithwaite, C.J.R. and **Zedef, V.** (1996) Hydromagnesite stromatolites and sediments in an alkaline lake, Salda Gölü, Turkey. *J. Sed. Res.*, **66**, 991–1002.

Bruker AXS (2004) Topas V.3.0: general profile and structural analysis software for powder diffraction data. Bruker AXS, Germany, Powder Diffraction.

Bruker AXS (2008) *DIFFRACplus EVA 14 Release 2008*. Karlsruhe, Germany.

Cerling, T.E., **Harris, J.M.**, **MacFadden, B.J.**, **Leakey, M.G.**, **Quade, J.**, **Eisenmann, V.** and **Ehleringer, J.R.** (1997) Global vegetation change through the Miocene/Pliocene boundary. *Nature*, **389**, 153–158.

Christ, C.L. and **Hostetler, P.B.** (1970) Studies in the system $MgO-SiO_2-CO_2-H_2O$ (II): the activity-product constant of magnesite. *Am. J. Sci.*, **268**, 439–453.

Clague, J.J., **Evans, S.G.**, **Rampton, V.N.** and **Woodsworth, G.J.** (1995) Improved age estimates for the White River and Bridge River tephras, western Canada. *Can. J. Earth Sci.*, **32**, 1172–1179.

Coshell, L., **Rosen, M.R.** and **McNamara, K.J.** (1998) Hydromagnesite replacement of biomineralized aragonite in a new location of Holocene stromatolites, Lake Walyungup, Western Australia. *Sedimentology*, **45**, 1005–1018.

Craig, H. (1961) Isotopic variations in meteoric waters. *Science*, **133**, 1702–1703.

Croizé, D., **Bjørlykke, K.**, **Jahren, J.** and **Renard, F.** (2010) Experimental mechanical and chemical compaction of carbonate sand. *J. Geophys. Res.-Solid Earth*, **115**, B11204.

Cummings, J.M. (1940) Saline and hydromagnesite deposits of British Columbia. *British Columbia Department of Mines*, Bulletin 4, 160 pp.

Das Sharma, S., **Patil, D.J.** and **Gopalan, K.** (2002) Temperature dependence of oxygen isotope fractionation of CO_2 from magnesite-phosphoric acid reaction. *Geochim. Cosmochim. Acta*, **66**, 589–593.

De Choudens-Sánchez, V. and **González, L.A.** (2009) Calcite and aragonite precipitation under controlled instantaneous supersaturation: elucidating the role of $CaCO_3$ saturation state and Mg/Ca ration on calcium carbonate polymorphism. *J. Sed. Res.*, **79**, 363–376.

Deines, P. (2004) Carbon isotope effects in carbonate systems. *Geochim. Cosmochim. Acta*, **68**, 2659–2679.

Deocampo, D.M. and **Ashley, G.M.** (1999) Siliceous islands in a carbonate sea: modern and Pleistocene spring-fed wetlands in Ngorongoro Crater and Oldupai Gorge, Tanzania. *J. Sed. Res.*, **69**, 974–979.

Détriché, S., **Bréhéret, J.G.**, **Karrat, L.**, **Hinschberger, F.** and **Macaire, J.J.** (2013) Environmental controls on the Late Holocene carbonate sedimentation of a karstic lake in the Middle-Atlas Mountains (Lake Afourgagh, Morocco). *Sedimentology*, **60**, 1231–1256.

Downes, H. (1985) Evidence for magma heterogeneity in the White River Ash (Yukon Territory). *Can. J. Earth Sci.*, **22**, 929–934.

Environment Canada (n.d.) National climate archive. Available at: www.climate.weatheroffice.ec.gc.ca (accessed August 17, 2012).

Eren, M. and **Hatipoglu-Bagci, Z.** (2010) Karst surface features of the hard laminated crust (caliche hardpan) in the Mersin area, southern Turkey. *Acta Carsologica*, **39**, 93–102.

Esteban, M. (1976) Vadose pisolite and caliche. *AAPG Bull.*, **60**, 2048–2057.

Fallon, S.J., **Fifield, L.K.** and **Chappell, J.M.** (2010) The next chapter in radiocarbon dating at the Australian National University: status report on the single stage AMS. *Nucl. Instrum. Meth. Phys. Res. Sect. B-Beam Interact. Mater. Atoms*, **268**, 898–901.

Gibson, J.J., **Edwards, T.W.D.**, **Bursey, G.G.** and **Prowse, T.D.** (1993) Estimating evaporation using stable isotopes – quantitative results and sensitivity analysis for 2 catchments in northern Canada. *Nord. Hydrol.*, **24**, 79–94.

Goldhammer, R.K. (1997) Compaction and decompaction algorithms for sedimentary carbonates. *J. Sed. Res.*, **67**, 26–35.

Grant, B. (1987) Magnesite, brucite and hydromagnesite occurrences in British Columbia. Open File Report of the British Columbia Geological Survey Branch, no. 1987-13.

Hänchen, M., **Prigiobbe, V.**, **Baciocchi, R.** and **Mazzotti, M.** (2008) Precipitation in the Mg-carbonate system – effects of temperature and CO_2 pressure. *Chem. Eng. Sci.*, **63**, 1012–1028.

Hancock, J.M., **McNeill, A.M.**, **McDonald, G.K.** and **Holloway, R.E.** (2011) Fate of fertiliser N applied to wheat on a coarse textured highly calcareous soil under simulated semi-arid conditions. *Plant Soil*, **348**, 139–153.

Hansen, L.D. (2005) *Geologic Setting of Listwanite, Atlin, B.C.: Implications for Carbon Dioxide Sequestration and Lode-gold Mineralization*. The University of British Columbia, Vancouver.

Hansen, L.D., **Dipple, G.M.**, **Gordon, T.M.** and **Kellett, D.A.** (2005) Carbonated serpentinite (listwanite) at Atlin, British Columbia: a geological analogue to carbon dioxide sequestration. *Can. Mineral.*, **43**, 225–239.

Harrison, A.L., **Power, I.M.** and **Dipple, G.M.** (2013) Accelerated carbonation of brucite in mine tailings for carbon sequestration. *Environ. Sci. Technol.*, **47**, 126–134.

Hopkinson, L., **Rutt, K.** and **Cressey, G.** (2008) The transformation of nesquehonite to hydromagnesite in the system $CaO-MgO-H_2O-CO_2$: an experimental spectroscopic study. *J. Geol.*, **116**, 387–400.

Hopkinson, L., **Kristova, P.**, **Rutt, K.** and **Cressey, G.** (2012) Phase transitions in the system $MgO-CO_2-H_2O$ during CO_2 degassing of Mg-bearing solutions. *Geochim. Cosmochim. Acta*, **76**, 1–13.

Hosseinpur, A.R., **Kiani, S.** and **Halvaei, M.** (2012) Impact of municipal compost on soil phosphorus availability and mineral phosphorus fractions in some calcareous soils. *Environ. Earth Sci.*, **67**, 91–96.

Jin, J.S. and Bergman, K.M. (1999) Sequence stratigraphy of the Middle Devonian Winnipegosis carbonate-prairie evaporite transition, southern Elk Point Basin. *Carbonates Evaporites*, **14**, 64–83.

Kaźmierczak, J., Kempe, S., Kremer, B., López-García, P., Moreira, D. and Tavera, R. (2011) Hydrochemistry and microbialites of the alkaline crater lake Alchichica, Mexico. *Facies*, **57**, 543–570.

Keeling, C.D., Bollenbacher, A.F. and Whorf, T.P. (2005) Monthly atmospheric $^{13}C/^{12}C$ isotopic ratios for 10 SIO stations. In: *Trends: A Compendium of Data on Global Change.* U.S. Department of Energy, Oak Ridge National Laboratory, Carbon Dioxide Information Analysis Center, Oak Ridge, TN.

Keppel, M.N., Post, V.E.A., Love, A.J., Clarke, J.D.A. and Werner, A.D. (2012) Influences on the carbonate hydrochemistry of mound spring environments, Lake Eyre South region, South Australia. *Chem. Geol.*, **296**, 50–65.

Kholodov, V.N. (2007) Caliches: a newly-formed boundary carbonate material in soils. *Lithol. Mineral Resour.*, **42**, 246–256.

Kim, S.T., O'Neil, J.R., Hillaire-Marcel, C. and Mucci, A. (2007) Oxygen isotope fractionation between synthetic aragonite and water: influence of temperature and Mg^{2+} concentration. *Geochim. Cosmochim. Acta*, **71**, 4704–4715.

Köhler, P., Hartmann, J. and Wolf-Gladrow, D.A. (2010) Geoengineering potential of artificially enhanced silicate weathering of olivine. *Proc. Natl Acad. Sci. USA*, **107**, 20228–20233.

Königsberger, E., Königsberger, L. and Gamsjager, H. (1999) Low-temperature thermodynamic model for the system Na_2CO_3-$MgCO_3$-$CaCO_3$-H_2O. *Geochim. Cosmochim. Acta*, **63**, 3105–3119.

Lackner, K.S., Wendt, C.H., Butt, D.P., Joyce, E.L., Jr and Sharp, D.H. (1995) Carbon dioxide disposal in carbonate minerals. *Energy*, **20**, 1153–1170.

Lahav, O., Morgan, B.E. and Loewenthal, R.E. (2001) Measurement of pH, alkalinity and acidity in ultra-soft waters. *Water SA*, **27**, 423–431.

Lakeman, T.R., Clague, J.J., Menounos, B., Osborn, G.D., Jensen, B.J.L. and Froese, D.G. (2008) Holocene tephras in lake cores from northern British Columbia, Canada. *Can. J. Earth Sci.*, **45**, 935–947.

Land, L.S. (1998) Failure to precipitate dolomite at 25C from dilute solution despite 1000-fold oversaturation after 32 years. *Aquat. Geochem.*, **4**, 361–368.

Last, W.M. (1992) Petrology of modern carbonate hardgrounds from East Basin Lake, a saline maar lake, southern Australia. *Sed. Geol.*, **81**, 215–229.

Last, W.M. (1993) Geolimnology of Freefight Lake: an unusual hypersaline lake in the northern Great Plains of western Canada. *Sedimentology*, **40**, 431–448.

Last, F.M. and Last, W.M. (2012) Lacustrine carbonates of the northern Great Plains of Canada. *Sed. Geol.*, **277**, 1–31.

Lerbekmo, J.F. (2008) The White River Ash: largest Holocene Plinian tephra. *Can. J. Earth Sci.*, **45**, 693–700.

Levson, V.M (1991). *Quaternary Geology of the Atlin Area (104N/11W, 12E).* British Columbia Geological Survey Branch.

Liutkus, C.M. and Wright, J.D. (2008) The influence of hydrology and climate on the isotope geochemistry of playa carbonates: a study from Pilot Valley, NV, USA. *Sedimentology*, **55**, 965–978.

Lopez, M., Gand, G., Garric, J., Körner, F. and Schneider, J. (2008) The playa environments of the Lodeve Permian basin (Languedoc-France). *J. Iberian Geol.*, **34**, 29–56.

McGlue, M.M., Ellis, G.S., Cohen, A.S. and Swarzenski, P.W. (2012) Playa-lake sedimentation and organic matter accumulation in an Andean piggyback basin: the recent record from the Cuenca de Pozuelos, North-west Argentina. *Sedimentology*, **59**, 1237–1256.

Mees, F., Castaneda, C. and Van Ranst, E. (2011) Sedimentary and diagenetic features in saline lake deposits of the Monegros region, northern Spain. *Catena*, **85**, 245–252.

Meister, P., Reyes, C., Beaumont, W., Rincon, M., Collins, L., Berelson, W., Stott, L., Corsetti, F. and Nealson, K.H. (2011) Calcium and magnesium-limited dolomite precipitation at Deep Springs Lake, California. *Sedimentology*, **58**, 1810–1830.

Melezhik, V.A., Fallick, A.E., Medvedev, P.V. and Makarikhin, V.V. (2001) Palaeoproterozoic magnesite: lithological and isotopic evidence for playa/sabkha environments. *Sedimentology*, **48**, 379–397.

Menounos, B., Osborn, G., Clague, J.J. and Luckman, B.H. (2009) Latest Pleistocene and Holocene glacier fluctuations in western Canada. *Quatern. Sci. Rev.*, **28**, 2049–2074.

Ming, D.W. and Franklin, W.T. (1985) Synthesis and characterization of lansfordite and nesquehonite. *Soil Sci. Soc. Am. J.*, **49**, 1303–1308.

Mook, W.G., Bommerson, J.C. and Staverman, W.H. (1974) Carbon isotope fractionation between dissolved bicarbonate and gaseous carbon dioxide. *Earth Planet. Sci. Lett.*, **22**, 169–176.

Nash, M.C., Troitzsch, U., Opdyke, B.N., Trafford, J.M., Russell, B.D. and Kline, D.I. (2011) First discovery of dolomite and magnesite in living coralline algae and its geobiological implications. *Biogeosciences*, **8**, 3331–3340.

Ohmoto, H. and Rye, R.O. (1979) Isotopes of sulfur and carbon. In: *Geochemistry of Hydrothermal Ore Deposits* (Ed. H.L. Barnes), 2nd edn, pp. 509–567. Wiley, New York, NY.

O'Neil, J.R. and Barnes, I. (1971) C^{13} and O^{18} compositions in some fresh-water carbonates associated with ultramafic rocks and serpentinites: western United States. *Geochim. Cosmochim. Acta*, **35**, 687–697.

Pakzad, H.R. and Kulke, H. (2007) Geomorphological features in the Gavkhoni playa lake, SE Esfahan, Iran. *Carbonates Evaporites*, **22**, 1–5.

Parkhurst, D.L. and Appelo, C.A.J. (1999) User's guide to PHREEQC (version 2) – a computer program for speciation, batch reaction, one-dimensional transport, and inverse geochemical calculations. U.S. Geological Survey Water-Resources Investigations Report 99-4259, 312 pp.

Peng, Q.M., Palmer, M.R. and Lu, J.W. (1998) Geology and geochemistry of the Paleoproterozoic borate deposits in Liaoning-Jilin, northeastern China: evidence of metaevaporites. *Hydrobiologia*, **381**, 51–57.

Poitevin, E. (1924) A new occurrence of lansfordite from Atlin, BC. *Am. Mineral.*, **9**, 225–228.

Power, I.M., Wilson, S.A., Thom, J.M., Dipple, G.M. and Southam, G. (2007) Biologically induced mineralization of dypingite by cyanobacteria from an alkaline wetland near Atlin, British Columbia, Canada. *Geochemical Trans.*, **8**, 13.

Power, I.M., Wilson, S.A., Thom, J.M., Dipple, G.M., Gabites, J.E. and Southam, G. (2009) The hydromagnesite playas of Atlin, British Columbia, Canada: a

biogeochemical model for CO_2 sequestration. *Chem. Geol.*, **260**, 286–300.

Power, I.M., Dipple, G.M. and Southam, G. (2010) Bioleaching of ultramafic tailings by *Acidithiobacillus* spp. for CO_2 sequestration. *Environ. Sci. Technol.*, **44**, 456–462.

Power, I.M., Wilson, S.A., Small, D.P., Dipple, G.M., Wan, W.K. and Southam, G. (2011) Microbially mediated mineral carbonation: roles of phototrophy and heterotrophy. *Environ. Sci. Technol.*, **45**, 9061–9068.

Power, I.M., Harrison, A.L., Dipple, G.M. and Southam, G. (2013a) Carbon sequestration via carbonic anhydrase facilitated magnesium carbonate precipitation. *Int. J. Greenhouse Gas Control*, **16**, 145–155.

Power, I.M., Harrison, A.L., Dipple, G.M., Wilson, S.A., Kelemen, P.B., Hitch, M. and Southam, G. (2013b) Carbon mineralization: from natural analogues to engineered systems. In: *Geochemistry of Geologic CO_2 Sequestration* (Eds D.J. DePaolo, D.R. Cole, A. Navrotsky and I.C. Bourg), *Rev. Mineral. Geochem.*, **77**, pp. 305–360. The Mineralogical Society of America, Chantilly, VA.

Power, I.M., Wilson, S.A. and Dipple, G.M. (2013c) Serpentinite carbonation for CO_2 sequestration. *Elements*, **9**, 115–121.

Raudsepp, M. and Pani, E. (2003) Application of Rietveld analysis to environmental mineralogy. In: *Environmental Aspects of Mine Wastes* (Eds J.L. Jambor, D.W. Blowes and A.I.M. Ritchie), **31**, pp. 165–180. Mineralogical Association of Canada, Ottawa.

Renaut, R.W. (1990) Recent carbonate sedimentation and brine evolution in the saline lake basins of the Cariboo Plateau, British Columbia, Canada. *Hydrobiologia*, **197**, 67–81.

Renaut, R.W. (1993) Morphology, distribution, and preservation potential of microbial mats in the hydromagnesite-magnesite playas of the Cariboo Plateau, British Columbia, Canada. *Hydrobiologia*, **267**, 75–98.

Renaut, R.W. and Long, P.R. (1989) Sedimentology of the saline lakes of the Cariboo Plateau, Interior British Columbia, Canada. *Sed. Geol.*, **64**, 239–264.

Renforth, P. (2012) The potential of enhanced weathering in the UK. *Int. J. Greenhouse Gas Control*, **10**, 229–243.

Renforth, P. and Manning, D.A.C. (2011) Laboratory carbonation of artificial silicate gels enhanced by citrate: implications for engineered pedogenic carbonate formation. *Int. J. Greenhouse Gas Control*, **5**, 1578–1586.

Richter, D.H., Preece, S.J., McGimsey, R.G. and Westgate, J.A. (1995) Mount Churchill, Alaska: source of the late Holocene White River Ash. *Can. J. Earth Sci.*, **32**, 741–748.

Romanek, C.S., Grossman, E.L. and Morse, J.W. (1992) Carbon isotopic fractionation in synthetic aragonite and calcite – effects of temperature and precipitation rate. *Geochim. Cosmochim. Acta*, **56**, 419–430.

Rubinson, M. and Clayton, R.N. (1969) Carbon-13 fractionation between aragonite and calcite. *Geochim. Cosmochim. Acta*, **33**, 997–1002.

Russell, M.J., Ingham, J.K., Zedef, V., Maktav, D., Sunar, F., Hall, A.J. and Fallick, A.E. (1999) Search for signs of ancient life on Mars: expectations from hydromagnesite microbialites, Salda Lake, Turkey. *J. Geol. Soc. London*, **156**, 869–888.

Saldi, G.D., Schott, J., Pokrovsky, O.S., Gautier, Q. and Oelkers, E.H. (2012) An experimental study of magnesite precipitation rates at neutral to alkaline conditions and 100-200 degrees C as a function of pH, aqueous solution composition and chemical affinity. *Geochim. Cosmochim. Acta*, **83**, 93–109.

Santos, G.M., Southon, J.R., Druffel-Rodriguez, K.C., Griffin, S. and Mazon, M. (2004) Magnesium perchlorate as an alternative water trap in AMS graphite sample preparation: a report on sample preparation at KCCAMS at the University of California, Irvine. *Radiocarbon*, **46**, 165–173.

Schuiling, R.D. and Krijgsman, P. (2006) Enhanced weathering: an effective and cheap tool to sequester CO_2. *Climatic Change*, **74**, 349–354.

Sipilä, J., Teir, S. and Zevenhoven, R. 2008. Report 2008–1 – carbon dioxide sequestration by mineral carbonation: literature review update 2005–2007. Åbo Akademi University Heat Engineering Laboratory.

Spencer, R.J., Baedecker, M.J., Eugster, H.P., Forester, R.M., Goldhaber, M.B., Jones, B.F., Kelts, K., McKenzie, J., Madsen, D.B., Rettig, S.L., Rubin, M. and Bowser, C.J. (1984) Great Salt Lake, and precursors, Utah: the last 30,000 years. *Contrib. Mineral. Petrol.*, **86**, 321–334.

Spotl, C. and Burns, S.J. (1994) Magnesite diagenesis in redbeds: a case study from the Permian of the Northern Calcareous Alps (Tyrol, Austria). *Sedimentology*, **41**, 543–565.

Spötl, C., Unterwurzacher, M., Mangini, A. and Longstaffe, F.J. (2002) Carbonate speleothems in the dry, inneralpine Vinschgau Valley, northernmost Italy: witnesses of changes in climate and hydrology since the last glacial maximum. *J. Sed. Res.*, **72**, 793–808.

Stamatakis, M.G., Renaut, R.W., Kostakis, K., Tsivilis, S., Stamatakis, G. and Kakali, G. (2007) The hydromagnesite deposits of the Atlin area, British Columbia, Canada, and their industrial potential as fire retardant. In: *Proceedings of the 11th International Congress*, *Bull. Geol. Soc. Greece*, **VII**, 10 pp.

Tarutani, T., Clayton, R.N. and Mayeda, T.K. (1969) The effect of polymorphism and magnesium substitution on oxygen isotope fractionation between calcium carbonate and water. *Geochim. Cosmochim. Acta*, **33**, 987–996.

Valero-Garcés, B.L., Delgado-Huertas, A., Navas, A., Machín, J., González-Sampériz, P. and Kelts, K. (2000) Quaternary palaeohydrological evolution of a playa lake: Salada Mediana, central Ebro Basin, Spain. *Sedimentology*, **47**, 1135–1156.

Vance, R.E., Mathewes, R.W. and Clague, J.J. (1992) 7000 year record of lake-level change on the northern Great Plains: a high-resolution proxy of past climate. *Geology*, **20**, 879–882.

Vasconcelos, C., McKenzie, J.A., Warthmann, R. and Bernasconi, S.M. (2005) Calibration of the delta $\delta^{18}O$ paleothermometer for dolomite precipitated in microbial cultures and natural environments. *Geology*, **33**, 317–320.

Walter, L.M., Bischof, S.A., Patterson, W.P. and Lyons, T.W. (1993) Dissolution and recrystalization in modern shelf carbonates: evidence from pore water and solid phase chemistry. *Phil. Trans. Roy. Soc. London Ser. A: Math. Phys. Eng. Sci.*, **344**, 27–36.

Washbourne, C.L., Renforth, P. and Manning, D.A.C. (2012) Investigating carbonate formation in urban soils as a method for capture and storage of atmospheric carbon. *Sci. Total Environ.*, **431**, 166–175.

Wilson, S.A., Raudsepp, M. and Dipple, G.M. (2006) Verifying and quantifying carbon fixation in minerals from serpentine-rich mine tailings using the Rietveld method

with X-ray powder diffraction data. *Am. Mineral.*, **91**, 1331–1341.

Wilson, S.A., **Dipple, G.M.**, **Power, I.M.**, **Thom, J.M.**, **Anderson, R.G.**, **Raudsepp, M.**, **Gabites, J.E.** and **Southam, G.** (2009a) Carbon dioxide fixation within mine wastes of ultramafic-hosted ore deposits: examples from the Clinton Creek and Cassiar chrysotile deposits, Canada. *Econ. Geol.*, **104**, 95–112.

Wilson, S.A., **Raudsepp, M.** and **Dipple, G.M.** (2009b) Quantifying carbon fixation in trace minerals from processed kimberlite: a comparative study of quantitative methods using X-ray powder diffraction data with applications to the Diavik Diamond Mine, Northwest Territories, Canada. *Appl. Geochem.*, **24**, 2312–2331.

Wilson, S.A., **Barker, S.L.L.**, **Dipple, G.M.** and **Atudorei, V.** (2010) Isotopic disequilibrium during uptake of atmospheric CO_2 into mine process waters: implications for CO_2 sequestration. *Environ. Sci. Technol.*, **44**, 9522–9529.

Wilson, S.A., **Dipple, G.M.**, **Power, I.M.**, **Barker, S.L.L.**, **Fallon, S.J.** and **Southam, G.** (2011) Subarctic weathering of mineral wastes provides a sink for atmospheric CO_2. *Environ. Sci. Technol.*, **45**, 7727–7736.

Young, G.A. (1916) Hydromagnesite deposits of Atlin, B.C. Geological Survey of Canada, Summary Report, 50–61.

Zedef, V., **Russell, M.J.** and **Fallick, A.E.** (2000) Genesis of vein stockwork and sedimentary magnesite and hydromagnesite deposits in the ultramafic terrans of southwestern Turkey: a stable isotope study. *Econ. Geol.*, **95**, 429–446.

Zhang, P., **Anderson, H.L.J.**, **Kelly, J.W.**, **Krumhansl, J.L.** and **Papenguth, H.W.** (2000) *Kinetics and Mechanisms of Formation of Magnesite from Hydromagnesite in Brine.* Sandia National Laboratories, Albuquerque.

Zheng, Y.F. (1999) Oxygen isotope fractionation in carbonate and sulfate minerals. *Geochem. J.*, **33**, 109–126.

Supporting Information

Additional Supporting Information may be found in the online version of this article:

Table S1. $\delta^{13}C$ and $\delta^{18}O$ values of the carbonate sediments of profiles 1 through 7 and lansfordite hardpan (this study) as well as aragonite from the main wetland and sediments from the grassland at depth (data from Power *et al.*, 2009). These data were converted to $\delta^{13}C$ values of the dissolved inorganic carbon (DIC) and $\delta^{18}O$ values of the water from which these carbonate sediments would have precipitated from based on equilibrium fractionation. Fractionation factors are based on the molar ratios of carbon and oxygen and the mineralogical proportions listed. See Fig. 11 for plots of the data.

Table S2. Equilibrium carbon and oxygen isotopic fractionation between carbonate minerals and bicarbonate and water, respectively. Weighted averages for fractionation factors listed in Table S1 were based on the molar ratios of carbon and oxygen for the mineral constituents based on mineral abundance data.

Table S3. Stable δ^2H, $\delta^{18}O$ and $\delta^{13}C$ values of the water samples collected from the Atlin site. Data are plotted in Fig. 3.

Figure S1. (A–C) Representative scanning electron micrographs of volcanic ash particles in profile 4 sediments; note the presence of vesicles (arrows). (D) Total alkali-silica diagram and representative SEM micrograph (E) of White River Ash. For comparison, data for the White River Ash from Downes (1985), Béget *et al.* (1992), Richter *et al.* (1995) and Lakeman *et al.* (2008) are also plotted.

Figure S2. Representative scanning electron micrographs of diatom frustules in Ca–Mg-carbonate sediments (A, B) and from the glaciolacustrine sediments (C).